Journal of Materials Chemistry B

ROYAL SOCIETY OF CHEMISTRY

PAPER

View Article Online
View Journal | View Issue

Cite this: J. Mater. Chem. B, 2025, 13, 6177

Synergistic photothermal and photodynamic therapy to promote bacteria-infected wound healing using ZnO@PDA/Ag-integrated waterborne polyurethane films†

Negar Salehi,[a] Abbas Mohammadi,*[a] Vajihe Alinezhad,[bc] Shayesteh Bochani,[c] Ali Kalantari-Hesari,[d] Fakhri Haghi,[e] Francisco Javier Sierra Valdez,[f] Tomás Jafed Buenfil-Chi,[g] Aziz Maleki*[ch] and Saeed Beigi-Boroujeni*[f]

Light-induced antibacterial effects aim to overcome the limitations of antibiotic-resistant bacteria and provide an effective solution for wound healing applications. This research focuses on developing a multifunctional wound dressing based on waterborne polyurethane (WPU) adorned with a hybrid photo nano-sensitizer (ZnO@PDA/Ag) that demonstrates near-infrared (NIR)-triggered synergistic photothermal and photodynamic effects. Through a facile synthesis process, zinc oxide (ZnO) nanoparticles were coated with polydopamine (PDA) to enhance biocompatibility, photothermic effect, and charge transfer efficiency due to a surface sensitization and passivation strategy. The synthesis was followed by the *in situ* reduction and decoration of plasmon silver nanoparticles (Ag NPs) to augment photodynamic activity. The structure, chemical composition, and morphology of the ZnO@PDA/Ag nano-sensitizer were examined and the results confirmed the successful synthesis. Furthermore, based on photothermal and fluorescence signal measurements under near-infrared (NIR) irradiation, the ZnO@PDA/Ag nanoparticles in aqueous dispersions exhibit effective light-to-heat conversion, as well as a strong ability for NIR-induced singlet oxygen generation. The WPU films incorporating the ZnO@PDA/Ag nano-sensitizer exhibit complete phototherapy inhibition of both Gram-negative *E. coli* and Gram-positive *S. aureus* bacteria. In addition, the films exhibited an appropriate biocompatibility in contact with L929 fibroblast cells. Moreover, *in vivo* studies in a rat wound model demonstrated accelerated wound healing and tissue regeneration with the application of ZnO@PDA/Ag in WPU nanocomposite film, particularly under NIR light irradiation. Histological analysis confirmed the formation of mature epithelial layers and minimal inflammatory response, indicating the potential of this film for clinical wound management.

Received 7th February 2025,
Accepted 19th April 2025

DOI: 10.1039/d5tb00277j

rsc.li/materials-b

1. Introduction

Antimicrobial phototherapy, particularly photodynamic therapy (PDT)[1] and photothermal therapy (PTT), has shown great potential in overcoming the problems regarding antibiotic-resistant pathogens.[2] Generally, PTT and PDT are minimally invasive phototherapeutic modalities for combating microbial infections[3,4] and treating cancer diseases.[5] The light interaction with the respective photo-agents can produce localized hyperthermia (>50 °C) or reactive oxygen species (ROS) in PTT and PDT, respectively.[6–9] An ideal photo-agent should have some special characteristics such as biocompatibility, stability, a large absorption coefficient for optical wavelengths within the biological tissue transparency window (700–1400 nm), and appropriate photothermal transduction efficiency.[7]

A wide range of near-infrared (NIR) photoabsorbers including nanoparticles (transitional metals and carbon nanomaterials),

[a] Department of Chemistry, University of Isfahan, Isfahan 81746-73441, Iran. E-mail: a.mohammadi@sci.ui.ac.ir
[b] Pharmaceutical Sciences Research Center, Institute of Herbal Medicines and Metabolic Disorders, Mazandaran University of Medical Sciences, Sari, Iran
[c] Department of Pharmaceutical Nanotechnology, School of Pharmacy, Zanjan University of Medical Sciences, 45139-56184 Zanjan, Iran. E-mail: maleki@zums.ac.ir
[d] Department of Pathobiology, Faculty of Veterinary Medicine, Bu-Ali Sina University, Hamedan, Iran
[e] Department of Microbiology, School of Medicine, Zanjan University of Medical Sciences, Zanjan, Iran
[f] School of Engineering and Sciences, Tecnológico de Monterrey, Ave. Eugenio Garza Sada 2501 Sur, Col Tecnologico, Monterrey, 64700, N.L., Mexico. E-mail: Saeed.beigi@tec.mx
[g] Centro de Investigación y de Estudios Avanzados-Monterrey, Parque de Investigación e Innovación Tecnológica, Apodaca, 66600, N.L., Mexico
[h] Zanjan Pharmaceutical Nanotechnology Research Center (ZPNRC), Zanjan, Iran

† Electronic supplementary information (ESI) available. See DOI: https://doi.org/10.1039/d5tb00277j

and semiconducting organic polymers (polydopamine, porphyrins, polyaniline, cyanines, and polypyrrole) have already been exploited to develop antibiotic-free photothermal wound dressings for bacteria-infected wounds.[2,8,10,11] Nevertheless, the single antibacterial modality exhibited limitations in achieving satisfactory therapeutic effects. For instance, single modality PTT may require high temperatures (>50 °C) to eliminate the bacterial population, that can result in undesired overheating injuries of healthy tissue.[12,13] To overcome these limitations, multifunctional synergistic therapeutics have been introduced by combining PTT with other approaches like PDT and sonodynamic therapy (SDT)[14–17]

The nanotechnology-based combinatorial PTT/PDT therapies have provided opportunities to enhance the advantages and avoid the drawbacks of the monotherapeutic approaches.[18] Hence, multifunctional nanotherapeutic platforms have largely been designed for treating bacterial infection and cancer cells *via* photodynamic/photothermal synergism by decorating ions, metals, polymer chains, and photosensitizers on semiconductors such as ZnO.[19,20]

ZnO is among the most used photoinduced antibacterial semiconductors due to its intrinsic antibacterial activity, photothermal property, and ROS generating ability. Nevertheless, its application in the biological window wavelength range (700 nm to 1000 nm), as an appropriate and safe light range with sufficient penetration depth in tissue sites, has been limited due to a wide bandgap (3.37 eV), low charge separation efficiency, and thereby fast electron–hole recombination.[21] Recently, various approaches, including surface plasmon modification, bandgap engineering, surface sensitization, and photon up-conversion, have been broadly studied to improve the light-harvesting ability of traditional semiconductors by extending light absorption into the NIR region.[22] Among them, the localized surface plasmon resonance (SPR) effect and surface sensitization can transfer the photo-excited electrons to the conduction band of semiconductors, leading to harnessing of the visible and NIR light adsorption by semiconductors.[22–24]

For instance, it has been proved that the decoration of the ZnO with plasmonic noble metal nanoparticles such as silver and gold NPs could circumvent the drawbacks by forming the potential energy barrier at the metal–semiconductor junction which enhanced the photogenerated charge separation, improving the photocatalytic activity under longer wavelength light.[20,25] On the other hand, various chromophore molecules and compounds have been used to enhance the light-harvesting ability of conventional semiconductors through surface sensitization.[26] In comparison to other photosensitizers such as organometallic complexes and organic dyes, semiconducting organic polymers like polydopamine (PDA) provide greater stability under photoirradiation.[24] PDA as a stable photosensitizer with a broad-spectrum visible-NIR light adsorption, is also well known for mimicking the extraordinary adhesion ability of the secreted marine mussel adhesive proteins due to the catechol and primary amine functional groups.[27,28] Therefore, the alkaline-triggered oxidative self-polymerization of dopamine has extensively been used for surface modification of a wide range of organic/inorganic substrates and nanoparticles.[29] In this respect, the formed surface-adherent PDA nanocoating not only served as a green reductant for the metal precursor to nanoparticles, but also acted as a linking agent to anchor and stabilize the *in situ* formed nanoparticles.[30,31] The biocompatibility, biodegradability, antibacterial and antioxidant properties, cell adhesion, hemostatic abilities, cell growth stimulation, biomimetic nature, and versatility of polydopamine (PDA) make it an ideal material for accelerating full-thickness wound regeneration.[32]

Furthermore, the intrinsic photothermal capability and semiconducting activity of PDA improve the photocatalytic performance of the photoactive agents.[33] However, polydopamine-coated photo-agents may exhibit uneven distribution within the coating matrix due to poor interfacial compatibility between the modified nanoparticles and the polymeric matrix. This non-uniform dispersion can lead to inconsistent temperature dissipation and/or ROS generation, potentially hindering effective antibacterial activity.[34,35]

Waterborne polyurethane (WPU) is an ideal polymeric matrix for integrating ZnO@PDA/Ag nanoparticles due to its unique physicochemical properties. As an aqueous dispersion, WPU provides a favorable environment for maintaining the stability and uniform distribution of nanoparticles, preventing aggregation and ensuring consistent photothermal and photodynamic activity. Compared to traditional solvent-based polymers, WPU offers significant advantages, including its environmentally friendly nature, as it does not require toxic organic solvents, thereby reducing potential cytotoxicity and environmental hazards. Moreover, WPU-based wound dressings have garnered increasing attention due to their excellent biocompatibility, low volatile organic compound (VOC) content, and tunable mechanical properties that allow for flexibility and durability. Its intrinsic hydrophilicity enhances nanoparticle dispersion and facilitates strong adhesion to biological tissues, promoting effective interaction at the wound interface. Additionally, WPU exhibits optimal water adsorption and vapor permeability (WVP), which are essential for maintaining a moist wound-healing environment while preventing excessive exudation buildup. The combination of these properties makes WPU a superior candidate for advanced antibacterial coatings in wound care applications.[36–38] Lu *et al.* encapsulated black phosphorus quantum dots within anionic waterborne polyurethane (WPU-BPQDs) to generate a PDT/PTT agent for cancer therapy. They observed a notable improvement in PDT under a 660 nm laser and PTT under an 808 nm laser in both *in vitro* and *in vivo* experiments with WPU-BPQDs.[39] Nevertheless, despite recent advancements in designing photothermally and photodynamically active WPU-based wound dressings, creating a single-NIR light-triggered synergistic PTT/PDT therapeutic system remains a worthwhile prospect.

In this study, a ternary photocatalyst (ZnO@PDA/Ag) was designed to harness NIR light for synergistic photodynamic/photothermal effects. The developed hybrid photocatalyst integrates the surface plasmon resonance of Ag NPs with the sensitization and passivation effects of PDA, while ZnO acts

as a photothermal agent and active site to facilitate plasmon-generated charge separation and enhance ROS production. PDA nanocoating was applied to ZnO *via* alkaline-triggered self-polymerization of dopamine, followed by *in situ* Ag deposition *via* catechol-coordinated reduction. The resulting ZnO@PDA/Ag nano-sensitizer was incorporated into a WPU dispersion to develop a multimodal antibacterial wound dressing.

To our knowledge, this is the first study employing ZnO@PDA/Ag for synergistic photothermal and photodynamic antibacterial therapy in WPU dressings. The decorated Ag NPs on the surface enhance the photodynamic activity of ZnO by improving the photogenerated charge separation that thereby hinders the recombination of photogenerated electron–hole pairs. On the other hand, the PDA nanocoating serves as favorable nucleation and anchor sites for Ag NPs and as an electron mediator with the latent photothermal activity. Compared to bare ZnO, the ZnO@PDA/Ag nano-sensitizer exhibited significantly higher singlet oxygen generation under NIR irradiation, promoting antibacterial efficacy and accelerating wound healing. Notably, wounds treated with ZnO@PDA/Ag-incorporated WPU dressings under NIR exposure showed the best wound closure effect after four days of *in vivo* healing.

2. Experimental

2.1. Materials

Waterborne polyurethane (WPU) was synthesized by using the following reagents: poly(ethylene adipate) (PEA, M_w = 1000 g mol^{-1}, Merck), isophorone diisocyanate (IPDI, Aldrich), dimethylolpropionic acid (DMPA, Aldrich), 1,4-butanediol (BDO, Aldrich), hexamethylenediamine (HMDA, Aldrich), trimethylamine (TEA, Merck), and acetone (Merck). The chemicals employed in the synthesis of nano-sensitizers are as follows: zinc chloride ($ZnCl_2$, Merck), sodium hydroxide (NaOH), propanol (C_3H_7OH), dopamine hydrochloride (4-(2-aminoethyl)-1,2-benzenediol, Aldrich), tris-(hydroxymethyl) aminomethane (Tris, Aldrich), and silver nitrate ($AgNO_3$, Merck).

2.2. Preparation of zinc oxide (ZnO) nanoparticles

First, $ZnCl_2$ was mixed with 200 mL of distilled water under an oil bath at 90 °C for 2.5 hours to dissolve completely. NaOH solution (5 M. 16 mL) was then added dropwise and stirred for 10 minutes. When the temperature of the solution dropped slightly, the precipitate was filtered off and dried at room temperature. The precipitate was washed 3 times with water, then the dried precipitate was dispersed in propanol (28.5 mL) and sonicated. The resulting solution was washed with propanol and finally centrifuged. The white precipitate was dried in an oven at 200 °C for 6 hours.

2.3. Preparation of ZnO@PDA

The schematic representation of the synthesis process for the hybrid photo nano-sensitizer (ZnO@PDA/Ag) is illustrated in Fig. 1a. To prepare ZnO@PDA, initially, ZnO (0.25 g) was dispersed in 90 mL of distilled water in an ultrasonic bath. Dopamine (0.2 g) was then dissolved in 10 mL of water and added to the ZnO dispersion under stirring. The pH was adjusted to 8.5 using a Tris buffer solution (0.04 M). The mixture was stirred at room temperature for 24 hours. Then, it was centrifuged to separate the solid product. The solid product was then washed to remove any impurities and finally dried at 50 °C to obtain the final ZnO@PDA product.

2.4. Preparation of ZnO@PDA/Ag nanoparticles

ZnO@PDA powder was dispersed in 40 mL of distillated water. Afterward, silver nitrate dissolved in 10 mL of water was add to the ZnO@PDA aqueous dispersion and stirred for 48 h at room temperature until the silver was well reduced. Then the reaction mixture was centrifuged and dried at 50 °C.

2.5. Synthesis of WPU and the WPU/NP dispersion

The illustration in Fig. 1b depicts the synthesis process of WPU. First, PEA (5 mmol), IPDI (12 mmol), and DMPA (2 mmol) were dissolved in 2 mL of acetone and added to a 250 mL three-neck round bottom flask equipped with a mechanical stirrer, condenser, and heated at 80° with stirring at a speed of 100 rpm in a nitrogen atmosphere for 2 h to synthesize the NCO-terminated polymer. BDO (4 mmol) was then added to the prepolymer mixture for over 30 minutes at 80 °C. The mixture was then cooled to 30 °C and TEA (4.3 mmol) was added to neutralize DMPA acid groups and stirred for 30 °C.[40] Finally, 20 mL HMDA solution (0.06 M) was added to the flask, and the mixture was vigorously stirred (500 rpm) for 30 minutes to obtain a WPU dispersion (solid content of 30%). To prepare the WPU/NP dispersions, the synthesized ZnO@PDA/Ag nanoparticles (3.75 mg) were first dispersed in deionized water (1.5 cc) using ultrasonication for 10 minutes to obtain a homogeneous suspension. The prepared nanoparticle dispersion was then added dropwise to the WPU dispersion (5 cc) under magnetic stirring at 200 rpm. The mixing continued for 24 hours to ensure complete incorporation of the nanoparticles into the WPU matrix (Fig. 1c).

2.6. Preparation of the WPU films

The WPU and WPU/NP films were prepared by casting the respective dispersions onto Teflon molds, followed by slow evaporation of the solvents at room temperature for 24 hours (Fig. 1c). According to the calculations, the weight percentage of nanoparticles in the WPU/NP film was set to 0.25%. Table 1 summarizes the coding and formulation details of all the prepared samples.

2.7. Characterization and properties

2.7.1. Characterization of the prepared nanoparticles. FTIR spectroscopy of ZnO, ZnO@PDA, and ZnO@PDA/Ag nanocomposites was performed on a JASCO FTIR-4600 spectrophotometer. XRD measurements were carried out at 25 °C on a Bruker D8 Advance diffractometer using CuKα radiation (λ = 1.540598 Å) with a scan rate of 1° min^{-1} between 2θ = 5° and 2θ = 80°. The morphology of nanoparticles was evaluated by scanning electron microscopy (SEM) using a scanning electron microscope (Thermo Fisher Scientific, Hillsboro, OR, USA).

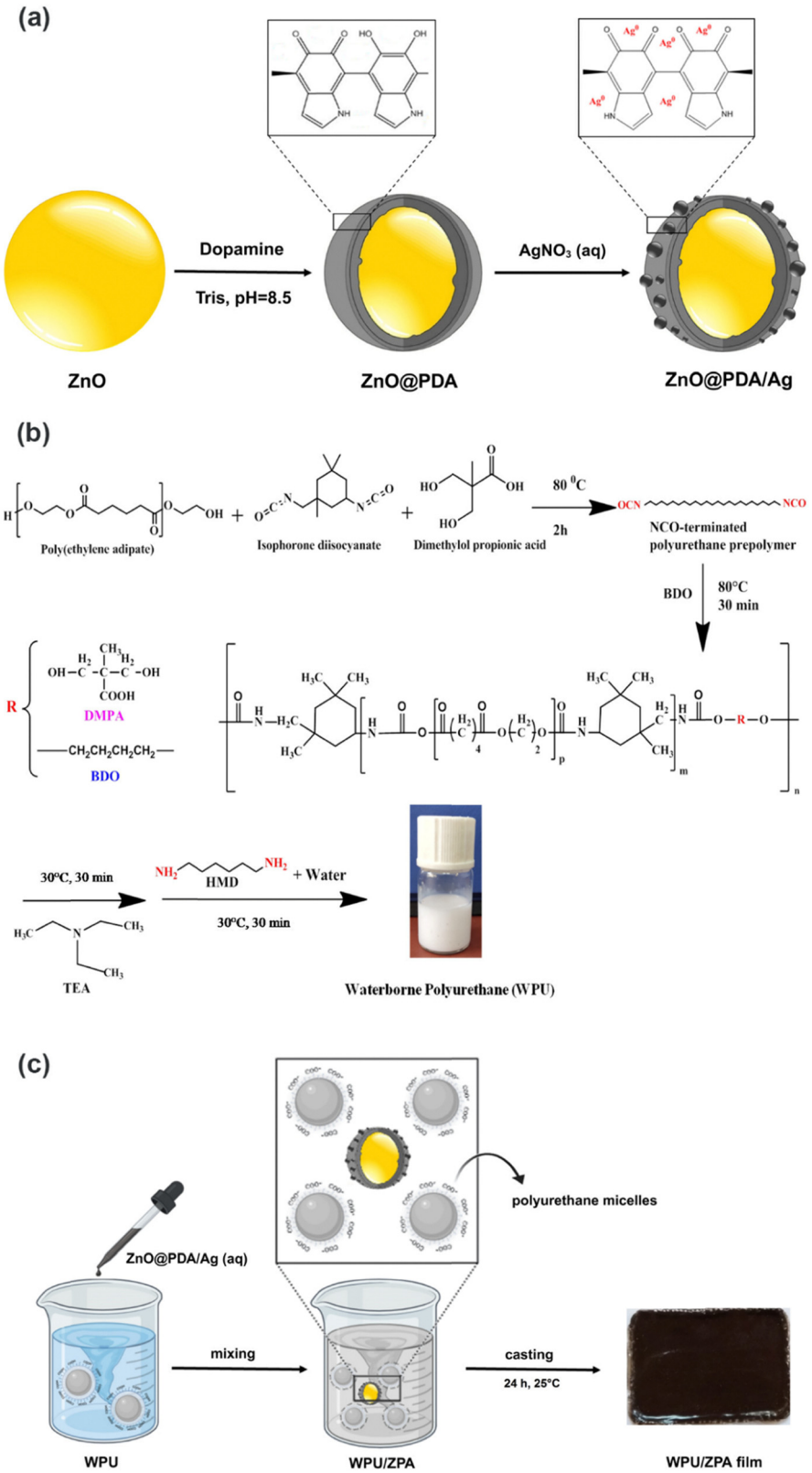

Fig. 1 Schematic preparation of the (a) ZnO@PDA/Ag NPs, (b) WPU dispersion, and (c) WPU/ZPA film.

HRTEM analysis was used to evaluate the morphology and size of silver nanostructures (Carl Germany, Oberkochen, Zeiss). X-ray photoelectron spectroscopy (XPS) was carried out on the UHV analysis system XPS spectrometer (FlexPS, SPECS). After being

Table 1 Coding and formulation of the prepared WPU and WPU/NP aqueous dispersions

Sample	Code name	Molar ratio (PEA : IPDI : DMPA : BDO : HMDA)	Stability	NP content in WPU dispersion (g L^{-1})	NP concentration in WPU film (wt%)
WPU	WPU	1 : 2.5 : 0.5 : 0.75 : 0.25	Stable	0	0
WPU/ZnO	WZ		Coagulated	1.25	0.25
WPU/ZnO@PDA	WZP		Stable	1.25	0.25
WPU/ZnO@PDA/Ag	WZPA		Stable	1.25	0.25

subjected to an X-ray bombardment, the sample's surface electrons were excited and expelled. An electron kinetic energy detector counted the number of electrons that were expelled from the sample surface and recorded the electrons' kinetic energy.

2.7.2. Characterization of the prepared WPU and WPU/NP dispersion. The mean particle size and the particle size distribution of the WPU and WPU/NPs were measured by a Horiba SZ-100 dynamic light scattering (DLS) instrument at room temperature. Zeta potentials of the WPU and WPU/NP dispersions were also measured at 25 °C.

2.7.3. Physicochemical characterizations of the prepared WPU and WPU/NP films. The microstructure of the polyurethane films and dispersion quality of NPs within the WPU/NP matrices were investigated by scanning electron microscopy (SEM) using a scanning electron microscope (Thermo Fisher Scientific, Hillsboro, OR, USA). HRTEM analysis was used to evaluate the morphology and size of silver nanostructures prepared in the presence of ZnO (Carl Germany, Oberkochen, Zeiss). Thermogravimetric analyses (TGA) were performed on PerkinElmer pyris 1 (PerkinElmer) to measure the weight loss of the WPU and WPU/NP films under a nitrogen (N_2) atmosphere. Hence, the samples were heated from 30 °C to 500 °C with a heating rate of 10 °C min^{-1} under a N_2 atmosphere.

2.7.4. Photodynamic capability measurements. To assess the generation of reactive oxygen species (ROS) crucial for photodynamic therapy, we employed chemical probes: singlet oxygen sensor green (SOSG, Invitrogen, OR, USA) for singlet oxygen, hydroxyphenyl fluorescein (HPF, Invitrogen, OR, USA) for hydroxyl radicals, and dihydroethidium (DHE, Sigma-Aldrich, USA) for superoxide anions.

Each chemical probe had a specific excitation/emission (Ex/Em) wavelength: singlet oxygen sensor green (SOSG, 504/525 nm), hydroxyphenyl fluorescein (HPF, 490/515 nm), and dihydroethidium (DHE, 518/606 nm).[41] The nanoparticles were dispersed (0.0044 mg mL^{-1}) into the chemical probe's water solution of 120 mM and continuously irradiated with an 808 nm laser (1.0 W cm^{-2}) at 25 °C for 30 minutes. Dispersions were further characterized with a spectrofluorometer obtaining the fluorescence intensity in counts per second (CPS) as a function of wavelength. Depending on each chemical probe, the fluorescence intensity at the characteristic emission wavelength is obtained to finally calculate the relative change in the fluorescence intensity (RCFI). This parameter is calculated using eqn (1) where S_t is the fluorescence intensity at the specific irradiation time and S_0 is the fluorescence intensity at zero time as a control.

$$\mathrm{RCFI} = (S_t - S_0)/S_0 \times 100\%, \quad (1)$$

2.7.5. Temporal singlet oxygen emission. To particularly monitor the temporal singlet oxygen response a reported experimental setup was utilized.[42] The ZnO@PDA/Ag nanoparticles were dispersed (0.0044 mg mL^{-1}) into the SOSG water solution (120 mM) and irradiated with an 808 nm laser (1 W cm^{-2}) at 25 °C for 60 minutes. A converging lens (f = 75.0 mm, D = 25.4 mm) was used to expand and guide a collimated beam (3 mm of diameter) through one of the two transparent sides of the sample cuvette. A dichroic mirror (Thorlabs Inc., DMLP-900, Newton, NJ, US) was used to both reflect the beam laser to the sample and transmit the infrared signal coming from the sample towards a set of filters. Emitted NIR photons are first collimated by the same lens and then focused on the detector fiber by a final lens (f = 25.4, D = 25.4 mm). The collection scheme has been optimized to have the collection efficiency limited only by the numerical aperture and diameter of the multimode fiber of the detector (NA = 0.275, D = 62.5 μm). In this way, it is possible to collect photons from an area of approximately 0.025 mm^2 with an equivalent numerical aperture of 0.1. Finally, a band-pass filter tuned at 1270 nm (BPF2, Thorlabs Inc., FB-1300-12, Newton, NJ, US) and a long-pass filter with a cut-off wavelength of 1200 nm (LPF1, Thorlabs Inc., FEL-1200, Newton, NJ, US) reject all unwanted photons. The output signal is provided by a digital potentiometer which generates a digital pulse for each detected photon. The signal was collected up to 270 seconds, capturing the signal every 0.1 seconds.

2.7.6. Photothermal performance of the nanostructures. To evaluate the photothermal activity of ZPA, we tested 1 mL aqueous solutions at various concentrations (125, 250, and 500 μg mL^{-1}) and with differing power densities (500, 1000, and 1500 mW cm^{-2}) under 808 nm laser irradiation. The photothermal stability of ZPA was assessed through four on–off laser cycles to confirm its performance over repeated use. Additionally, the photothermal conversion efficiency (η) of both ZP and ZPA was determined following the method reported in ref. 43. Detailed procedures for these measurements can be found in the ESI.†

2.7.7. Photothermal performance of WPU and WZPA films. The photothermal activity of the as-prepared WPU and WZPA films (cubes 5 × 5 × 1 mm) was studied using 808 nm NIR laser irradiation (power density 1 W cm^{-2} for 8 min). The temperature was monitored using a digital thermal camera (TiS55, Fluke, USA).

2.7.8. *In vitro* antibacterial activity of WPU and WZPA. The spread plate method was used to study the antibacterial effect of WPU and WZPA. *Escherichia coli* (*E. coli*, ATCC25922) and

Staphylococcus aureus (*S. aureus*, ATCC25923) were used to assess the antibacterial activity of the films. The bacteria were cultured in brain heart infusion (BHI) broth/agar (Merck, Germany) for 18–24 h at 37 °C aerobically. 20 μL of the as-made bacterial suspension (1.5×10^8 CFU mL^{-1}) was added into 1 mL of normal saline containing the same amount of WPU and WZPA films (cubes $5 \times 5 \times 1$ mm) and normal saline without the films was used as the control group. The NIR-treated groups were exposed to 808 nm light for 10 min (1.0 W cm^{-2}). After 2 h incubation, the bacterial solution was re-suspended and diluted using normal saline 30 times. Next, 100 μL of the diluted bacterial solution was spread on the nutrient agar and incubated for 20–24 h.[44] Bacterial colonies were counted in each sample and the bacterial survival ratio was calculated as follows:

$$\text{Bacterial survival ratio (\%)} = (N \text{ in sample}/N \text{ in control}) \times 100 \quad (2)$$

where N displays the colony number on a plate.

2.7.9. *In vitro* cytotoxicity. The colorimetric MTT assay was employed to assess the cytocompatibility of the samples against mouse L929 fibroblast cells. Prior to the assay, the samples (5×5 mm^2) were sterilized by first immersing them in 70% ethanol for 3 minutes, followed by thorough washing with sterile phosphate buffer solution and drying. The sterilized samples were then exposed to UV light for 15 minutes. These sterilized samples were placed in 24-well plates containing 10^4 mouse L929 fibroblast cells per well. A well without a sample served as a control. The plates were incubated at 37 °C, 50% relative humidity, and 5% CO_2 for 1, 3, and 7 days. After the incubation period, the culture media was removed, and 500 μL of a 0.05 wt% MTT solution in sterile PBS was added to each well. The plates were incubated in the dark at 37 °C for 5 hours. Following incubation, the MTT solution was removed, and the formazan crystals formed by viable cells were dissolved in 500 μL of dimethyl sulfoxide. The absorbance of each well was measured at 570 nm using a microplate reader. The percentage of viable cells was calculated by comparing the absorbance of the sample groups to the control group.

2.7.10. *In vivo* wound healing study. A full-thickness cutaneous infected wound model was used to assess the healing performance of the films. All animal studies were approved by the animal research Bu Ali Sina University-Hamedan animal ethics committee (IR.BASU.REC.1402.0623). First, Sprague-Dawley rats (180–220 g) were randomly divided into four groups. Control. Tegaderm, WPU, WZPA and, WZPA (+NIR). The animals were anesthetized by intraperitoneal injection of ketamine (50 mg mL^{-1})-xylazine (20 mg mL^{-1}) (250 μL, 6 : 4 v/v) and then the dorsal region was shaved. A full-thickness wound (diameter: 1.2 cm) was created on each rat and 30 μL of *S. aureus* suspension ($\sim 10^8$ CFU mL^{-1}) was added to the wound sites subsequently. In the NIR-irradiated groups, each wound was exposed to an 808 nm laser (1 W cm^{-2}) after placing the films. The temperature of the wound site was monitored by infrared camera and maintained at 44 °C for 10 min. The repair process of wounds was evaluated by wound area calculations. The wounds were photographed on days 0, 3, 6, and 10. The films were replaced on the 3rd day. Wound closure was measured by Image J software according to the formula:[45]

$$\text{Wound area (\%)} = A_n/A_0 \times 100 \quad (3)$$

where, A_0 and A_n displayed the wound areas on day 0 and the other times, respectively.

2.7.11. Histopathological analysis. To evaluate epidermal regeneration and inflammation in the wound site, wound tissues were collected on the 3rd and 10th days. The skin tissues were fixed with 10% formaldehyde and the samples sectioned (5 μm thick slices) and, subsequently, stained with hematoxylin or eosin (H&E). The slices were monitored by a microscope, Dino-Lite camera and Dino-capture software (V.2).

2.7.12. Statistical analyses. The experimental data were expressed as ± standard error mean. The statistical analysis was carried out with a general linear model and one-way ANOVA followed by Bonferroni test for multiple comparisons and *t*-test. The p values were considered as $^{****}p < 0.0001$, $^{***}p < 0.001$, $^{*}p < 0.05$ for significant differences.

3. Results and discussion

3.1. Characterization of ZnO, ZnO@PDA, and ZnO@PDA/Ag nanoparticles

In the FTIR spectrum of ZnO nanoparticles, as depicted in Fig. 2a, the signal within the 400 to 500 cm^{-1} range corresponds to the stretching vibration of the Zn–O bond. Additionally, the broad peak at near 3400 cm^{-1} is attributed to the hydroxyl groups on the surface of ZnO nanoparticles.[46] Regarding the polydopamine modified zinc oxide nanoparticles, new peaks emerged at 1595 cm^{-1}, 1492 cm^{-1}, and 1293 cm^{-1}, indicating the presence of C═O, C═N or/and C═C, and C–O bonds associated with polydopamine, respectively.[47] Furthermore, the shift of the hydroxyl peak to 3300 cm^{-1} can be attributed to the inclusion of NH groups within the polydopamine structure.[48] In the case of ZnO@PDA/Ag nanoparticles, a decrease in the peak intensity of the Zn–O bond is observed, which can be attributed to the formation of silver nanoparticles on the surface of the ZnO nanoparticles.[46,49]

XRD analysis was used to evaluate the phase structure of bare ZnO, ZnO@PDA, and ZnO@PDA/Ag nanoparticles and the results are depicted in Fig. 2b. The XRD pattern of unmodified ZnO exhibited seven sharp 2θ peaks at 31.8°, 34.5°, 36.3°, 47.4°, 56.6°, 62.8°, and 68°,[50] corresponding to the crystalline structure of ZnO nanoparticles. Furthermore, the XRD pattern of ZnO@PDA nanoparticles was the same as that of unmodified ZnO nanoparticles. The polymerization of dopamine on the surface of ZnO nanoparticles resulted in a decrease in peak intensities, which is consistent with previous research findings.[46,51] The XRD diffraction pattern of ZnO@PDA/Ag nanoparticles exhibited new distinctive 2θ peaks (asterisk labeled) appeared at 38.2°, 44.4°, 64.5°, and 77.4°, corresponding well with the crystallographic planes of Ag nanoparticles.[52,53] On the other hand, the significant decrease of 2θ peak intensity related to ZnO in XRD

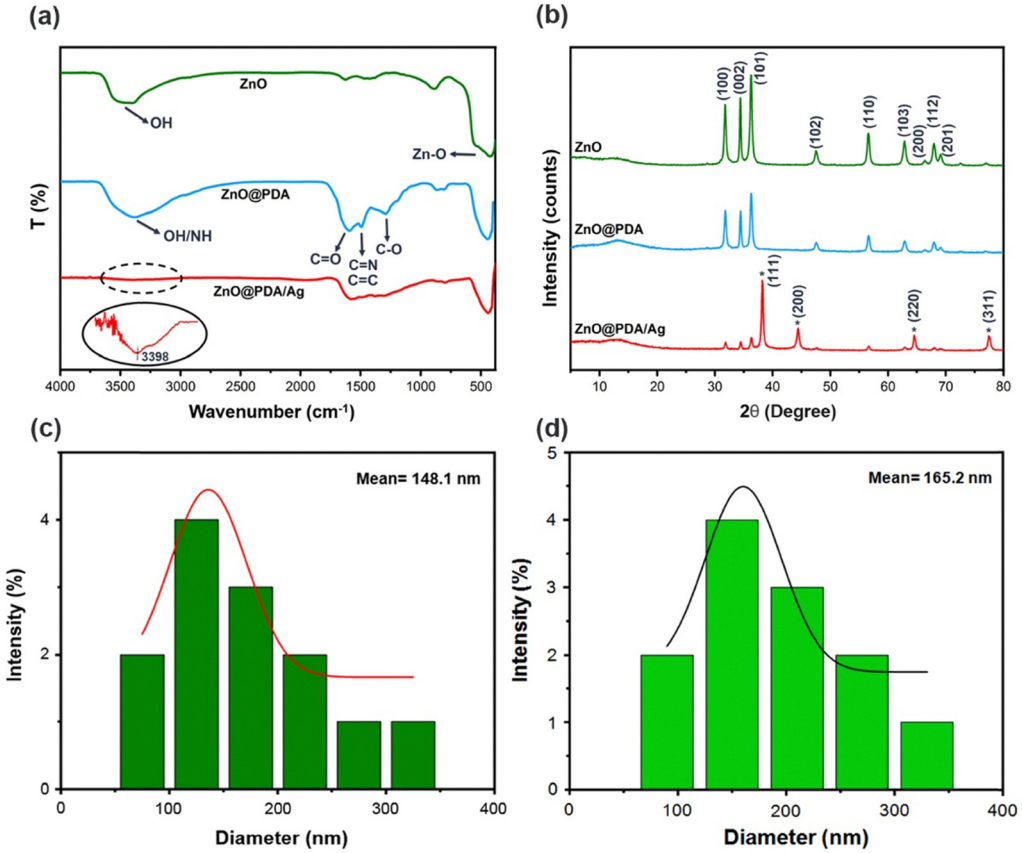

Fig. 2 (a) FTIR and (b) XRD analysis of ZnO, ZnO@PDA, and ZnO@PDA/Ag nanoparticles. DLS analysis of ZnO (c) and ZPA (d) aqueous dispersions.

diffractogram ZnO@PDA/Ag nanostructures, can be attributed to the formation of Ag NPs on the surface of ZnO particles.[54]

DLS was employed to assess the hydrodynamic size of the aqueous dispersion of nanoparticles. The histograms in Fig. 2c and d illustrate the distribution of hydrodynamic sizes for the ZnO and ZnO@PDA/Ag nanoparticles dispersed in water. The ZnO nanoparticles have an average hydrodynamic size of 148.1 nm, while the ZnO@PDA/Ag nanoparticles have an average hydrodynamic size of 165.2 nm. This increase in average size can be attributed to the coverage of the ZnO particles with a hydrophilic layer on the PDA/Ag nanostructures.

3.1.1. XPS analysis. The chemical composition of ZnO@PDA/Ag NPs and the valence state of their elements were further evaluated by X-ray photoelectron spectroscopy (XPS) analysis. Fig. 3a shows the wide scan survey spectra of ZnO@PDA/Ag NPs, in which the sharp peaks related to Zn, O, N, C, and Ag elements are marked. Fig. 3b displays the high resolution XPS spectrum of Zn 2p in two characteristic peaks located at 1022.5 and 1046.1 eV, attributing to the binding energies of Zn 2p3/2 and Zn 2p1/2, respectively. These results correspond to the typical binding energy values for ZnO.[55]

Fig. 3c shows the high-resolution X-ray photoelectron spectroscopy (XPS) spectrum of Ag 3d. The spectrum exhibits the spin–orbit splitting of Ag 3d into the Ag $3d_{3/2}$ (373.8 eV) and Ag $3d_{5/2}$ (368.5 eV) peaks, which indicates the successful reduction of silver ions to metallic Ag^0 species. This confirms the presence of Ag nanoparticles on the surface of the ZnO@PDA nanostructures. Additionally, the split between the Ag $3d_{3/2}$ and Ag $3d_{5/2}$ peaks is 6.0 eV, which further confirms the presence of metallic Ag in the ZnO@PDA/Ag nanostructures.[56] As shown in Fig. 3d, the representative high-resolution X-ray photoelectron spectroscopy (XPS) spectrum of the N 1s region is deconvoluted into three distinct peaks. These peaks are located at 398.6 eV, 399.9 eV, and 400.9 eV, which correspond to primary (R–NH_2), secondary (R–NH–R), and tertiary (=N–R) amine moieties, respectively. This deconvolution confirms the successful formation of the PDA coating on the surface of the ZnO nanoparticles.[57]

Although the detailed polymerization mechanism of dopamine has not been fully understood, there is evidence that dopamine undergoes a consecutive step of oxidation and rearrangement resulting in several tautomers of quinone and indole. These intermediate species held together covalently and/or noncovalently to form a polydopamine network.[27,58] So, according to the agreed contemporary polymerization mechanism of dopamine, the primary amine located at 398.6 eV can be attributed to the R–NH_2 of dopamine. However, the secondary and tertiary amines are mainly associated with tautomeric intermediate species of the dopamine and polydopamine network.[57] The spectrum of the C 1s region is deconvoluted into three peaks (Fig. 3e). The carbons doubly bonded to oxygen and nitrogen atoms are found in the intermediate/

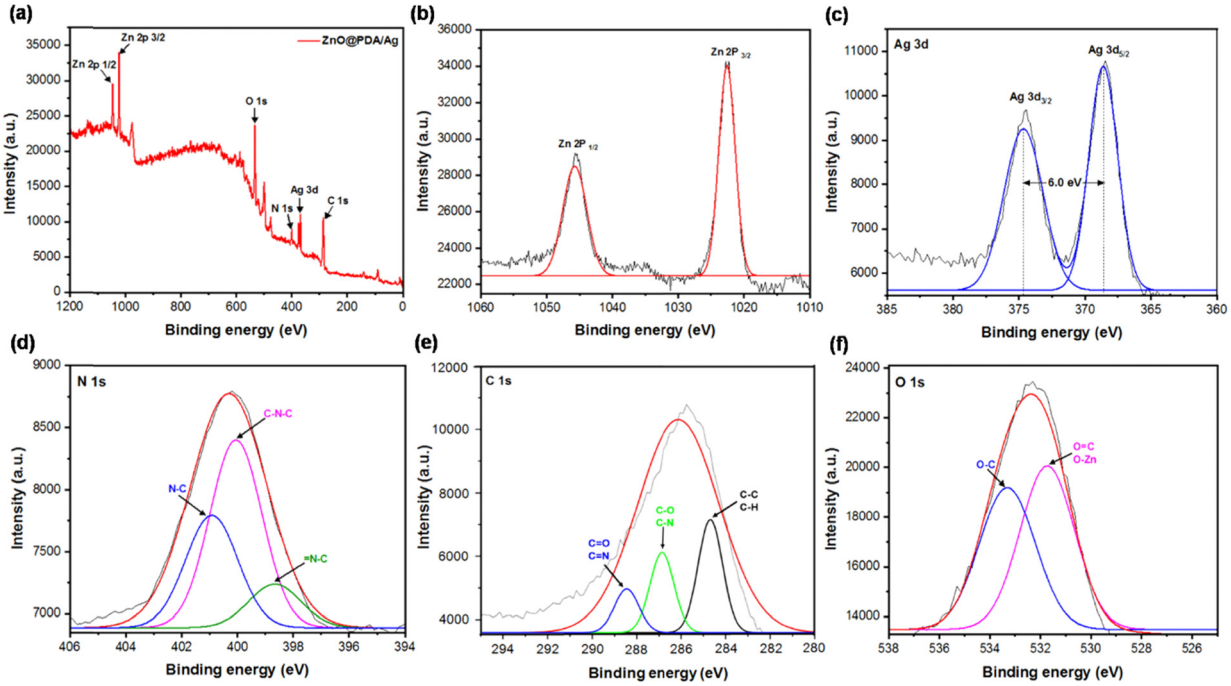

Fig. 3 X-ray photoelectron spectroscopy (XPS) data for the ZnO@PDA/Ag nanoparticles: (a) scan survey, (b) Zn 2p, (c) Ag 3d, (d) N 1s, (e) C1s, and (f) O1s.

tautomer species of dopamine, and the polydopamine network. This observation further confirmed the formation of PDA. The spectrum of the O 1s region is also fit with two peaks at 531.7 eV and 533.3 eV, assigned to C–C/C–H (284.5 eV), C–O/C–N (286.8 eV), and C═O/C═N (288.5 eV) species corresponding to the O–Zn/O═C and O–C bond energies (Fig. 3f). The O═C bond is found in both intermediate/tautomer species of dopamine, and the polydopamine network, whereas the O–C is mainly found in dopamine.[59,60]

3.1.2. SEM and TEM analysis. SEM and TEM analysis were employed to evaluate the morphology and the size of the nanoparticles. According to Fig. 4a, the high-magnification SEM micrograph exhibited the disk-shaped ZnO[61] particles with different size, ranging from approximately 120 to 180 nm, with an average size of 170 ± 0.5 nm. The larger nanoparticle sizes observed could be attributed to the formation of interconnected agglomerates between the nanoparticles. The SEM micrograph of ZnO@PDA/Ag nanoparticles exhibited also a rough surface, indicating the presence of Ag NPs. The elemental mapping of Ag and Zn within the highlighted area with a yellow-dotted line indicated a uniform distribution of Ag NPs on the surface of ZnO@PDA/Ag nanoparticles (Fig. 4b). The operation of SEM in the transmission mode (STEM) was performed for high-resolution imaging and Fig. 4c exhibits the dark-field STEM image of ZnO@PDA/Ag nanoparticles. Accordingly, the decorating silver nanoparticles with higher atomic number appeared bright on the surface of ZnO/PDA nanoparticles. The surface chemical composition of ZnO@PDA/Ag nanoparticles was assessed by the energy-dispersive X-ray spectroscopy (EDS) analysis coupled with STEM (Fig. 4d). This analysis showed a strong signal for the silver atoms at 3 keV, indicating a characteristic peak of metallic silver nanocrystals. Furthermore, the presence of Zn and O is confirmed by the energy peaks at 1 keV, 8.7 keV, and 0.5 keV, respectively.[62] EDX analysis of ZnO@PDA/Ag NPs confirmed the presence of C (15.35%), N (2.83%), O (18.78%), Zn (27.18%), and Ag (35.86%).

The morphology and particle size of the nanoparticles were further analyzed using HRTEM. In Fig. 4e, a typical single ZnO@PDA/Ag nanoparticle is depicted, revealing distinct boundaries between its three constituent parts. The ZnO core, measuring 94 nm in diameter, is disk-shaped and uniformly covered by a thin, brighter layer with a thickness of 24 nm, representing the PDA layer. Additionally, on the surface, there is an Ag NP, characterized by its quasi-spherical shape, black appearance, and a diameter of nearly 34.4 nm. Fig. 4f displays a TEM image showcasing agglomerated nanoparticles, while Fig. 4g presents the particle size histograms of Ag NPs with a mean size of 21 nm. Notably, the silver nanoparticles, predominantly spherical in shape and ranging from 10 to 35 nm, are distinctly visible in black on the zinc oxide nanoparticle surface. The occurrence of larger Ag nanoparticles on the ZnO surface could be due to the aggregation of smaller Ag nanoparticles. The particle size of ZPA observed through TEM and DLS closely aligns and exhibits consistency. However, DLS reported slightly larger measurements due to the highly hydrophilic nature of ZPA, resulting from the PDA layer, which promotes water absorption. This phenomenon commonly come about as DLS measures the hydrodynamic diameter, leading to reported sizes typically slightly larger than those from TEM.[40]

3.1.3. UV-visible absorption. In a PTT or PDT process, a thorough understanding of the absorption spectrum of the photo-agent is vital for selecting the appropriate light source and refining treatment parameters to achieve the desired

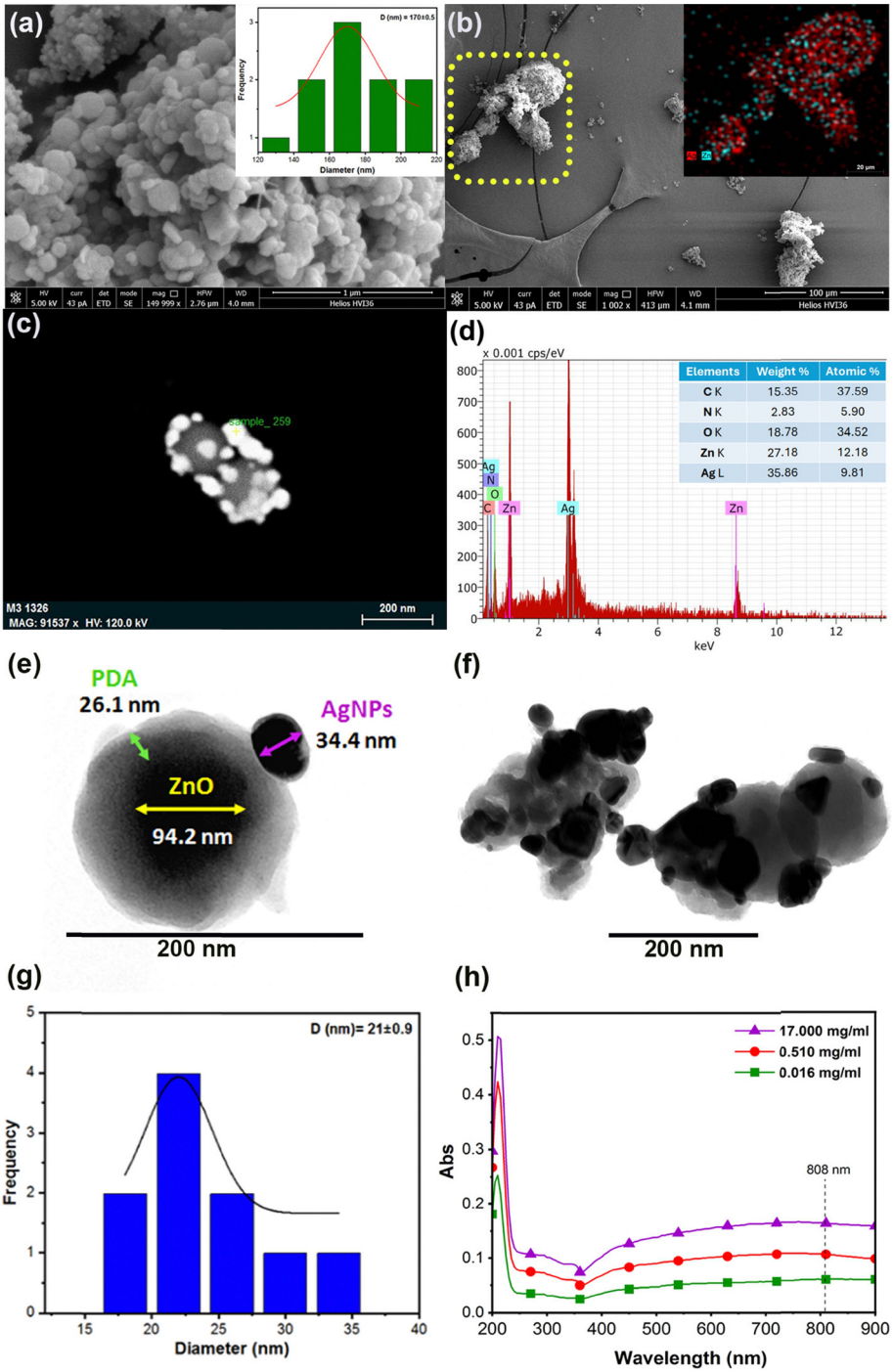

Fig. 4 (a) High-magnification SEM micrograph and size distribution of Zno@PDA/Ag nanoparticles and (b) EDX mapping of Ag and Zn within the highlighted area with a yellow-dotted line. (c) Dark-field STEM image of nanoparticles, and (d) EDX analysis of ZPA nanoparticles. (e) and (f) HRTEM images of ZnO@PDA/Ag nanoparticles, (g) particle size histograms of Ag nanoparticles, and (h) UV-vis absorption spectra of ZPA water dispersions at different concentrations.

therapeutic outcomes. The UV-vis absorbance of ZPA was analyzed to determine the light absorption characteristics. The UV-vis-NIR absorbance spectra of ZnO@PDA/Ag NPs (Fig. 4h) indicated absorption in the NIR region (700–900 nm), confirming the NIR activity of the NPs. It appears that absorption peaks of the ternary components merged, resulting in a broad absorption with low intensity within the range of 400–900 nm. The main reason behind the broadened absorption peak extending towards the longer wavelengths is likely the synergistic effect of the surface plasmon resonance of Ag NPs coupled with the surface sensitization/passivation of PDA. As observed, such an activity increased with higher concentrations of the ZPA NPs,

indicating that the photoactive properties of the NPs were concentration dependent.

3.1.4. Photodynamic capability. Fluorescent probes, as ROS sensitive molecules, were used to detect generated ROS. Generally, fluorescent probes are non-fluorescent molecules that can be rapidly and selectively oxidized by ROS to turn into highly fluorescent molecules with a strong fluorescence emission. For instance, SOSG, as a preferred fluorescent probe for singlet oxygen detection, is a two-component molecule in which a light-emitting fluorophore is coupled to an anthracene-derived trapping moiety (Fig. 5a). In the absence of singlet oxygen, the probe is in the "off" position due to quenching of the emission from the fluorophore through the photo-induced electron transfer from the adjacent substituted anthracene. In the presence of singlet oxygen, the anthracene-derived trapping moiety undergoes a chemical transformation, becoming an endoperoxide anthracene moiety. This transformation eliminates its ability to act as an intramolecular electron donor, effectively "turning on" the probe and resulting in fluorescence emission at approximately 525 nm.

Since each probe has a specific excitation/emission (Ex/Em) wavelength, the relative change in the fluorescence signal intensity of the aqueous ZnO@PDA/Ag nanoparticle dispersion containing the different probe molecules of SOSG, HPF, and DHE was monitored under different NIR irradiation time and the profiles depicted in Fig. 5a–c. As shown in Fig. 5d, the fluorescence intensity of DCF detected at 525 nm increases with longer irradiation time and exhibits a significant enhancement after NIR irradiation for 60 minutes. This observation exhibited an exclusive release of singlet oxygen species after 60 min of irradiation time. Nevertheless, the change in fluorescence intensity at 515 nm and 606 nm of HPF and DHE is negligible after NIR irradiation, indicating insufficient concentration of hydroxyl radicals and superoxide anions. Therefore, further studies on photodynamic experiments were focused on the generation of singlet oxygen species.

The NIR-induced singlet oxygen generation of ZnO, ZnO@PDA, and ZnO@PDA/Ag NP aqueous dispersions was evaluated and the relative change in the fluorescence signal intensity profiles at 0, 15, and 60 min of NIR irradiation for the nanoparticle dispersions is depicted in Fig. 5e. The fluorescence intensity increased with longer NIR irradiation time in three nanoparticle dispersions. Particularly, the signal intensity of singlet oxygen produced by the ZnO@PDA/Ag NP dispersion was substantially higher than that produced by other dispersions,

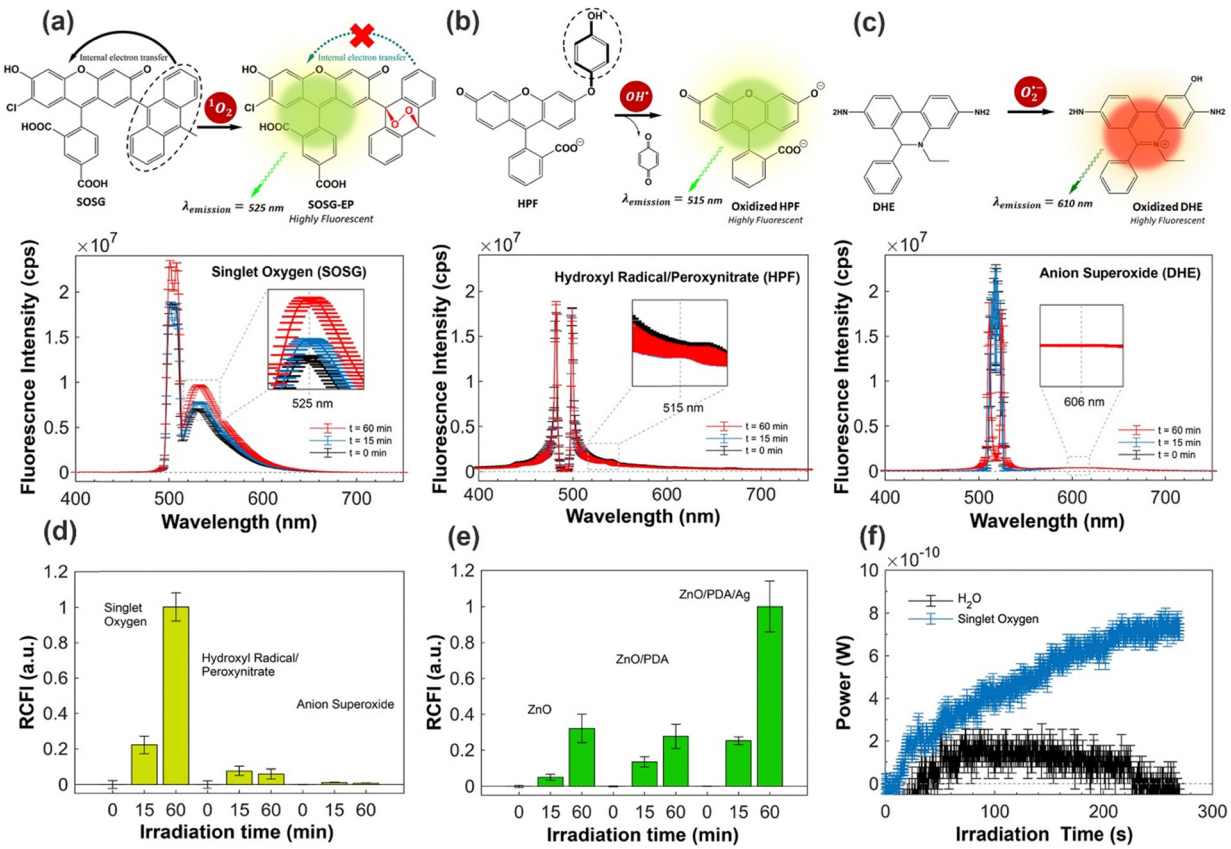

Fig. 5 Schematic performance images of fluorescent probes and fluorescence intensity profile for the aqueous ZnO@PDA/Ag nanoparticle dispersions containing the different fluorescent probes at 0, 15 and 60 min of irradiation: (a) singlet oxygen detection, (b) hydroxyl radical/peroxynitrate detection, and (c) anion superoxide. (d) Relative change in the fluorescence intensity (RCFI) profile collected from the fluorescence intensity profile of different fluorescent probes in Fig. 5a–c. (e) RCFI profile for singlet oxygen detection at 0, 15 and 60 min of irradiation for aqueous dispersions of ZnO NPs, ZnO/PDA NPs, and ZnO@PDA/Ag NPs containing singlet oxygen fluorescent probes. (f) Real-time monitoring of singlet oxygen production for an aqueous ZnO@PDA/Ag nanoparticle dispersion (blue) with respect to the water response (black) as a control.

suggesting that ZnO@PDA/Ag NPs had a strong ability for ROS generation.

Furthermore, the PDA coating could serve as a bridge between ZnO and Ag NPs. PDA has notable electron donor properties and can facilitate charge transfer pathways, aiding in the separation and migration of photoinduced electron–hole pairs.[63] This promotes efficient utilization of the photogenerated charges, reducing charge recombination and improving photocatalytic efficiency.

The exceptional release of singlet oxygen species of nanoparticle dispersion inspires us to monitor the real-time singlet oxygen production. Hence, the temporal singlet oxygen emission was detected using a solid-state detector (InGaAs). Fig. 5f exhibits the power intensity in real time excited at the appropriate wavelength. It is observed that, with respect to water, the immediate generation of $^1O_2$ is a continuously increasing signal, in which an expected reaching maximum value is due to a saturation in the power intensity approximately after 270 s in all the cases.

3.1.5. Photocatalytic and charge transfer mechanism. The mechanism for singlet oxygen generation by ZPA is proposed as shown in Fig. 6a and b.

Prior to contact, silver exhibits a higher Fermi energy compared to ZnO due to the latter's higher work function.[64] Upon contact, charge transfer and electrostatic effects lead to the establishment of a new, unified Fermi energy level.[65] This phenomenon, along with the incorporation of plasmonic Ag nanoparticles and a PDA ad-layer, enables ZnO@PDA/Ag to exhibit optical reactivity across a broader spectrum, extending from the visible to near-infrared (NIR) wavelengths, while still maintaining efficient photo-excitation of the wide band gap ZnO under UV light.[66] The NIR photon harvesting by PDA/Ag arises primarily from the induced surface plasmon resonance of the silver nanoparticles and secondly from the sensitizing and passivating effect of the PDA ad-layer.

The interaction of incident light with the surface free electrons on Ag NPs triggers collective oscillations of these electrons, generating an intense localized electromagnetic field known as surface plasmon resonance (SPR).[67] The dissipation of SPR energy through non-radiative processes can stimulate the generation of highly energetic plasmonic hot electrons. These hot electrons possess sufficient energy to transfer to the conductive band (CB) of the ZnO counterpart.[23] The PDA

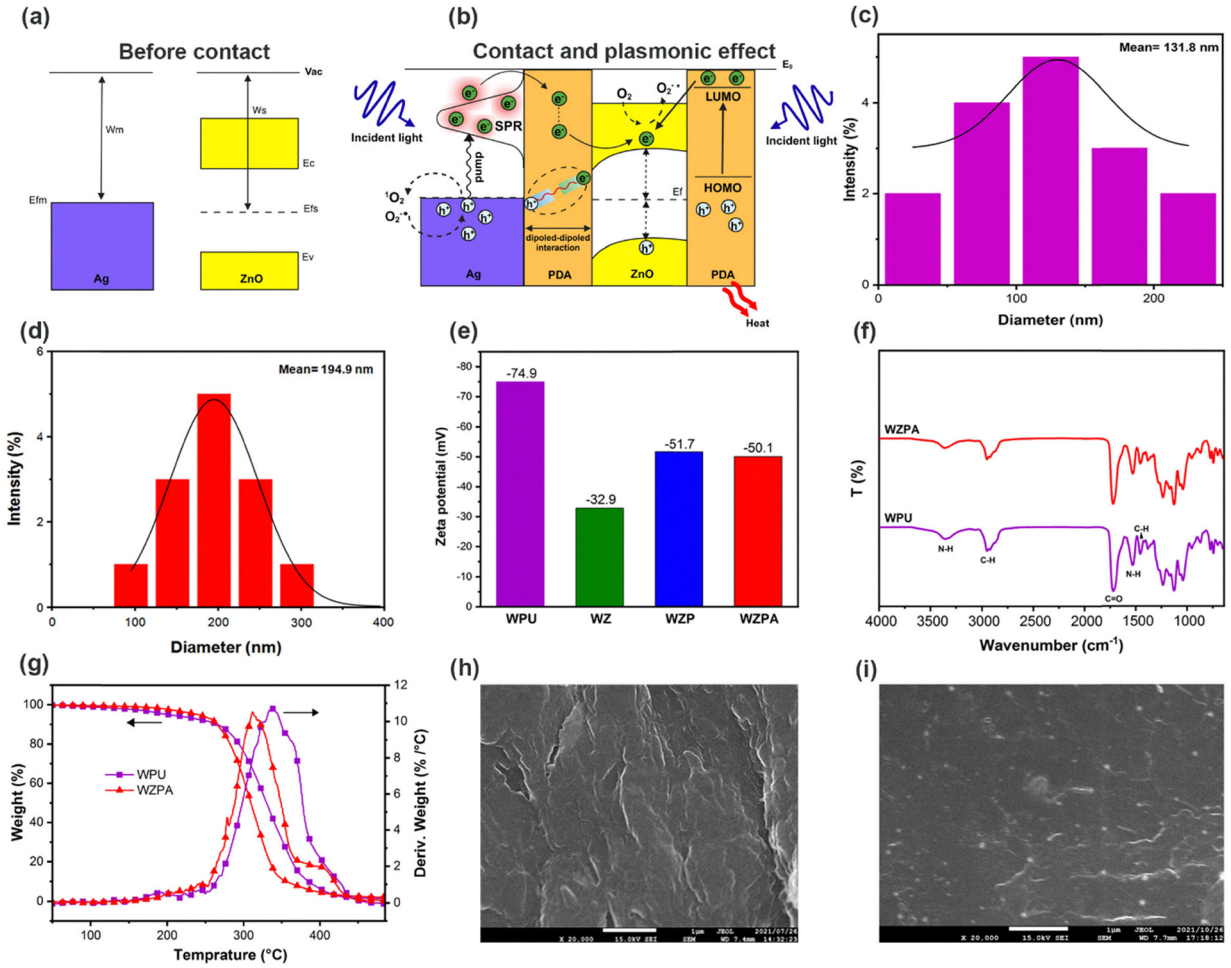

Fig. 6 Proposed schematic diagram of the photocatalytic mechanism of ZPA nanoparticles under NIR irradiation: (a) before and (b) after contact. (c) DLS analysis of WPU and (d) WZPA dispersions. (e) Zeta potential analysis of the prepared dispersions. (f) FTIR analysis of WPU and WZPA films. (g) Thermogravimetric analysis of WPU and WZPA films, TGA and DTG thermograms. (h) SEM images of WPU and (i) WZPA films.

ad-layer acts as an electron transfer mediator, facilitating the interfacial photo-induced electron transfer between Ag and ZnO. This enhances the separation efficiency of photo-generated carriers in Ag NPs.[68]

Since the conduction band-edge energy of ZnO (−0.363 eV *vs.* NHE) is lower than the $O_2/O_2^{-\bullet}$ reduction potential (−0.33 eV *vs.* NHE), electrons injected into the ZnO conduction band may be captured by adsorbed O_2 molecules to produce superoxide radical anions.[66] It is speculated that the formed $O_2^{-\bullet}$ might have potentially interacted directly with Ag NPs, undergoing oxidation by SPR-induced holes on Ag NPs.[69] Recent studies have highlighted that polymer ad-layers, such as PDA, can effectively passivate the plasmonic surface of Ag NPs, which significantly enhances the accumulation of hot electrons. This process helps to prevent the recombination of electron–hole pairs generated by surface plasmon resonance (SPR).[70] As a result, PDA plays a crucial role in promoting charge transfer by facilitating the efficient separation of photo-generated electrons (e^-) and holes (h^+). The separation of these charge carriers enables enhanced electron transfer from Ag^0 to the surface of ZnO, which is a critical step for improving photocatalytic activity. Additionally, PDA, with its organic semiconductor nature, not only enhances the electronic interactions between the Ag and ZnO but also helps to stabilize the reactive charge carriers, leading to better efficiency in photocatalytic reactions. These effects contribute to the overall improvement of the photocatalytic system by enhancing the generation and utilization of ROS. Furthermore, it has been proved that a PDA thin layer can serve as a photosensitizer coating, boosting light absorption and expediting the transfer of photogenerated electrons.[71] This enhancement consequently improves the photocatalytic performance of traditional semiconductors with wide bandgaps across the visible to near-infrared light spectrum.[24,72] When exposed to NIR light, the electrons located in the highest occupied molecular orbital (HOMO) of the ad-layer PDA are stimulated, prompting their transition to the lowest unoccupied molecular orbital (LUMO).[72] These photoelectrons are subsequently conveyed to the conduction band of ZnO, assisting the reduction of absorbed O_2 into superoxide radical anions.

3.1.6. Characterization of WPU dispersions and films. DLS and zeta potential measurements were employed to assess the hydrodynamic size and surface electric charge of the WPU dispersion with and without nanoparticles. The histogram in Fig. 6c illustrates the distribution of hydrodynamic sizes for WPU micelles, with an average size of 131.8 nm. Incorporation of ZPA nanoparticles in a WPU dispersion, as depicted in Fig. 6d, leads to larger diameters of 194.9 nm, attributed to the stacking of WPU chains around the nanoparticles. The zeta potentials of the WPU dispersion containing nanoparticles were also measured to evaluate their stability. Generally, the particles with zeta potential above +30 mV or below −30 mV are considered stable.[73] Consequently, as depicted in Fig. 6e, all dispersions exhibited excellent stability. The WPU dispersion showed excellent stability by displaying a significantly negative potential of −74.9 mV, indicating the hydrophilic character of the WPU micelle surface due to the existence of carboxylate groups in the polyurethane backbone. The WPU dispersion containing ZnO@PDA nanoparticles, exhibiting a zeta potential of −51.7 mV, displayed a substantial improvement in stability compared to the WPU dispersion containing ZnO, which had a zeta potential of −32.9 mV. As proven, the PDA can interact with the various substrates through different chemical groups. This characteristic facilitates its interaction with WPU micelles and enhances the dispersibility of nanoparticles. On the other hand, the WPU dispersion containing ZnO@PDA/Ag, with a zeta potential of −50.1 mV, showed no significant differences in terms of stability compared to the WPU dispersion with ZnO@PDA nanoparticles. This observation indicates that the introduction of Ag NPs did not substantially affect the stability of the WPU dispersion.

Fig. 6f shows the ATR-FTIR spectra of WPU films. The WPU sample is detected by the stretching vibrations of the N–H band (urethane) at 3327 cm^{-1} and the stretching vibrations of the carbonyl groups at 1710 cm^{-1}. Also, the absorption band at 1535 cm^{-1} is related to the out of plane N–H bending vibrations of urethane and urea.[74] Asymmetric and symmetric C–H stretching vibrations are also observed at 2935 and 2855 cm^{-1} respectively. The absorption bond at 1463 cm^{-1} is related to CH_2 bending vibrations and also C–N stretching vibrations appeared at 1365 cm^{-1}.[40] Furthermore, the complete consumption of isocyanate groups during the creation of WPU films is shown by the non-appearance of the absorption band associated with the stretching vibrations of the NCO group at 2270 cm^{-1}.[40] Almost no significant difference is observed in the FTIR spectrum of WPU and WZPA nanocomposite films, which is due to the small weight fraction of nanoparticles in the samples.

The thermogravimetric (TGA) and derivative thermogravimetric (DTG) thermograms of the samples are depicted in Fig. 6g. The thermal degradation of polyurethanes typically occurs in two stages. The first stage is related to the scission of urethane linkages in the hard segments, while the second degradation step is associated with the decomposition of the polyols in the soft segments.[36,40] According to the TGA thermograms, the WZPA nanocomposite film exhibited higher thermal stability compared to the neat WPU film. The onset temperature of degradation (T_{onset}) for the WZPA nanocomposite was 205 °C, whereas the neat WPU film had a lower T_{onset} of 155 °C. This suggests that the incorporation of ZnO@PDA/Ag (ZPA) nanoparticles into the WPU matrix led to strong interactions with the hard segments, which in turn decreased the chain mobility and required higher temperatures for polymer degradation.[26,39]

The DTG results showed a decrease in the thermal stability of the nanocomposite film at higher temperatures. This is indicated by the lower T_{max} (the maximum decomposition rate temperatures of the soft segments) of 315 °C for the WZPA nanocomposite film compared to the neat WPU film, which had a T_{max} of 345 °C. The thermal degradation of nanocomposites can be affected by the thermal catalysis performance of ZnO nanoparticles as an n-type semiconductor. The thermally

excited ZnO can accelerate the thermal decomposition process of polymers by generating free oxygen and proxy radicals through the polymeric lattice.[75] On the other hand, the thermal stability deterioration can also be attributed to the weakening of hydrogen bonds within the hard segments, which occurs due to the interaction of the polymer backbone with ZnO/PDA/Ag nanoparticles. It has been proved that the interaction of hard segments of polyurethane with functional groups on nanoparticle surfaces leads to a lower degree of crystallinity and phase separation.[76,77] In the present study, the existence of the PDA layer results in superficial hydroxyl/quinone moieties on ZnO, making the nanoparticles more capable of interacting with the polyurethane hard segments, ultimately resulting in smaller phase separation.

The surface morphology of films was investigated using SEM. Fig. 6h and i display SEM micrographs of WPU and WPU/NP films, respectively. The WPU film's surface shows a clear contrast between different regions, with some areas appearing bright and others appearing dark. This observation can be attributed to the microphase separation between hard and soft segments of the polyurethane backbone.[78] Accordingly, bright areas likely correspond to hard domains, while the dark areas represent soft domains within the WPU film. In contrast, the WZPA film exhibits fewer bright and dark regional lines, indicating a more uniform microstructure with reduced microphase separation. This can be attributed to the looser packing of hard segments caused by the accumulation of ZnO@PDA/Ag NPs on WPU molecular chains. As shown in Fig. 8a, white dots on the film's surface confirm the presence of ZnO@PDA/Ag NPs, which are uniformly distributed, suggesting effective nanoparticle dispersion within the film structure.

3.1.7. Photothermal activity of nanoparticles and their film composite. Photothermal therapy has been extensively developed as a safe and effective approach for bacterial elimination through heat production.[79,80] Using this method, a photothermal agent can absorb NIR light (700–1700 nm) to generate local heat. It has been reported that Ag and PDA nanoparticles acted as a photothermal agent.[81–84] As previously stated, the UV-visible-NIR absorbance spectra of ZnO@PDA/Ag nanoparticles exhibited absorption within the near-infrared (NIR) range of 700–900 nm, indicating the NIR functionality of the nanoparticles, which is an essential aspect to implement a photothermal therapeutic effect in biomedical applications. As shown in Fig. 7a, upon 808 nm laser irradiation, the temperature of aqueous ZPA solutions increased with rising nanoparticle concentrations, indicating a concentration-dependent heat generation. Besides, the temperature increased with increased light power density, highlighting power-dependent heat production (Fig. 7b). On the other hand, the ZPA NPs demonstrated excellent photothermal stability, as indicated by a consistent on–off thermal response during four temperature cycling tests (Fig. 7c). To evaluate the photothermal conversion efficiencies, the photothermal responses of ZP and ZPA nanoparticles were analyzed through a single heating–cooling cycle, as illustrated in Fig. S1 (ESI†). These data showed a strong linear correlation between the negative natural logarithm of temperature and cooling time, enabling the calculation of photothermal conversion efficiencies (η) for both materials. The calculated efficiencies were 14.8% for ZP and 31.0% for ZPA, indicating that these

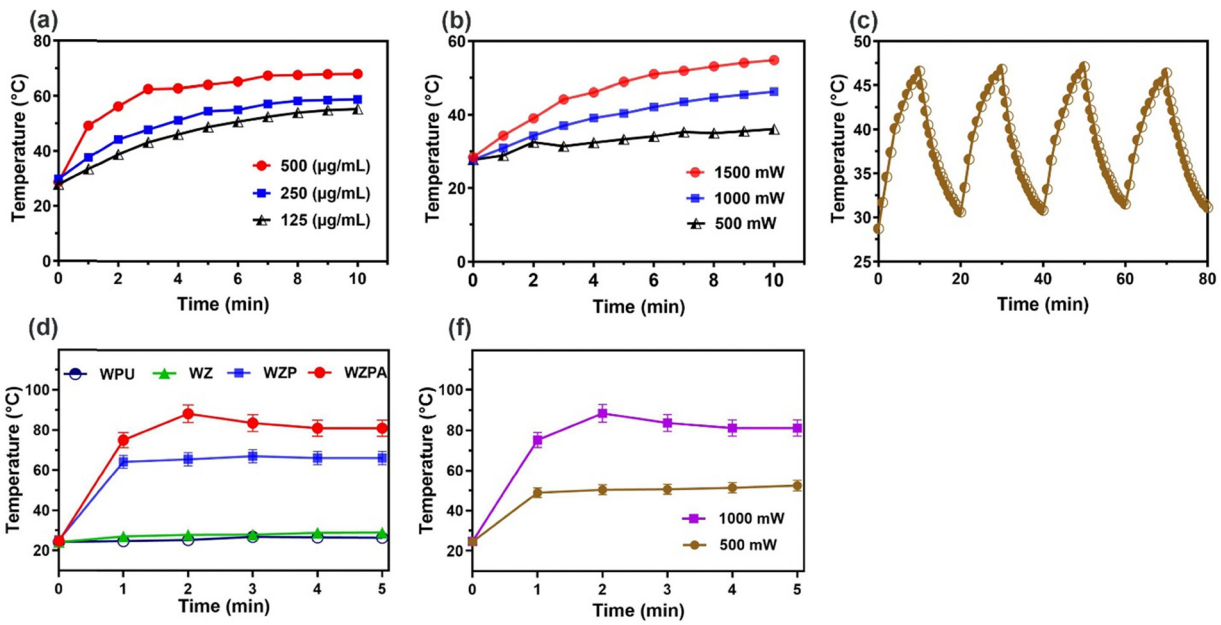

Fig. 7 (a) Temperature curves of ZPA NPs at different concentrations under 808 nm laser irradiation with a power density of 1.0 W cm^{-2}, (b) power dependency of the heat generation of ZPA (125 μg mL^{-1}), (c) the temperature *vs.* time curve for the ZPA NPs (125 μg mL^{-1}) irradiated with an 808 nm laser (1.0 W cm^{-2}) for four on/off cycles (on: 10 min, off: 10 min), (d) temperature increase profiles of the WZPA, WZP, WZ, and WPU films under 808 nm laser irradiation (1 W cm^{-2}), and (f) temperature elevation of the WZPA film at different powers of NIR light (808 nm).

values are sufficient to support effective photothermal therapy (PTT) applications.

Photothermal behavior of the WPU, WZ, WZP, and WZPA films was also evaluated by irradiation with an 808 nm NIR light (1 W cm^{-2}) and the results are depicted in Fig. 7d. As predicted, WPU and WZ did not show photothermal activity. In contrast, when ZnO@PDA and ZnO@PDA/Ag NP-loaded films, *i.e.*, WZP and WZPA, were irradiated by the NIR light a remarkable increase in the temperature occurred. As shown, after 5 min irradiation, WZPA showed a higher increase than the WZP, demonstrating higher potential ZnO@PDA/Ag NPs than the ZnO@PDA to act as a photothermal agent. Fig. 7f shows temperature changes of the WZPA film exposed to an 808 nm laser at power densities of 1000 mW and 500 mW, indicating the power dependency of the NIR-active film under the *in vitro* conditions. This observation confirmed the effective light-to-heat conversion capability of the WPZA nanocomposite film.

3.1.8. *In vitro* NIR-triggered antibacterial performance. Bacterial infection usually remains a big challenge during the wound healing process. Therefore, it is of particular importance to develop multifunctional systems with superior bactericidal performance.[85,86] *S. aureus* and *E. coli* belonging to Gram-positive bacteria and Gram-negative bacteria, respectively, were used to investigate the antibacterial properties of the WPU and WZPA with/without 808 nm laser irradiation using a spread plate method test (Fig. 8a–d). The control group showed a significant number of viable colonies on agar plates with/without NIR light. Although viable colony units decreased when WPU was used as an antibacterial agent, the bacterial survival (%) was not significant in comparison with the control group. In contrast, the groups treated with WZPA without NIR irradiation exhibited a significant decrease in the number of colonies which can be related to Ag ions released from the WZPA.[87] Interestingly, this decrease in bacterial viability was further increased in the presence of NIR light and even no bacteria colony was observed. According to the mechanism schematically depicted in Fig. 8f, the significant antibacterial efficacy of nanoparticles arises from the synergistic integration of photothermal effects, photodynamic properties, and Ag ion release of ZnO@PDA/Ag nanoparticles.[87–90] As previously mentioned, the WZPA has the capability to produce a significant amount of singlet oxygen when exposed to NIR light. Consequently, the resulting reactive oxygen species can penetrate into bacteria and trigger bacterial death through oxidative stress.[91] Furthermore, the nanoparticles exhibit enhanced photothermal properties due to the intense localized surface plasmon resonance (LSPR) of Ag NPs and the inherent photothermal activity of PDA under NIR light. This leads to a temperature rise of up to 45 °C, causing bacterial destruction by damaging intracellular proteins and the cellular membrane.[79,86] The thermal camera images captured during the bacteria killing process under NIR irradiation. These images clearly illustrate that the WZPA film experiences significant heating when exposed to NIR, whereas the WPU film shows no temperature increase under the same conditions (Fig. 8e). Such NIR irradiation led to temperature enhancements of 30.5 °C and 42.0 °C for WPU and WZPA, respectively. The hyperthermia could further increase the antibacterial effect of the multifunctional films.[12,92,93]

3.1.9. MTT assay. The MTT assay was performed to evaluate the biocompatibility of nanocomposite films by assessing the metabolic activity and proliferation of L929 fibroblast cells.[94] Fig. 8g shows the cell viability of the fibroblast cells on days 1, 3 and 7. The results showed that all prepared films demonstrated significantly higher cell viability compared to the control group ($p < 0.05$) after one day of incubation. This indicates that the films are non-toxic and support cell adhesion. Moreover, a significant increase in cell growth was observed on all films after 7 days of culture, with no evidence of cytotoxicity. These findings suggest that nanocomposite films are biocompatible and promote cell proliferation. Interestingly, the addition of ZnO@PDA nanoparticles enhanced cell growth on the surface of the WZP nanocomposite film, confirming the excellent biocompatibility of ZnO and PDA, which promote cell-surface interactions with the polymer.[95] Furthermore, the WZPA nanocomposite film containing silver nanoparticles exhibited a slight decrease in cell viability compared to the WZP film without silver nanoparticles. However, the WZPA film still demonstrated significantly higher cell viability compared to the control group ($p < 0.05$) after one, three, and seven days of incubation. This indicates that the WZPA film is non-toxic and supports cell adhesion, even with the presence of silver nanoparticles.

3.1.10. *In vivo* wound healing and histological studies. An SD rat model of *S. aureus*-infected wound was used to evaluate the effects of the developed photoactive PU-based dressings on wound healing *in vivo*. The incisional wounds were treated by the films and Tegaderm. Fig. 9a displays a representative digital image of the wounds in different groups. Compared to the Tegaderm group, the incisions treated by the NIR-active films showed improved wound closure effects, indicating excellent antibacterial and wound repair properties of the films. As shown, the WZPA groups exhibited the best wound healing results after 10 days of treatment. Utilizing wound photos taken at various intervals, quantifiable wound areas were calculated (Fig. 9b). On day 3, Tegaderm, WPU, WZPA (−NIR), and WZPA (+NIR) displayed wound areas of 91.97%, 91.04%, 91.72%, 72.96%, and 72.28% respectively. As shown, wound healing in the groups treated with WZPA (with/without NIR light) was significantly improved compared with commercial Tegaderm and control groups. The ability of the multifunctional films to act as a strong antibacterial agent and the healing effect of the polyurethane-based films can be the cause of this phenomenon.[79,84] In addition, our quantitative analysis showed that there was a significant difference in the wound area (%) between the control and WZPA (+ NIR) groups on day 6 ($^{*}p < 0.05$) and day 10 ($^{**}p < 0.01$). Such healing was further confirmed by our histological results (Fig. 9c).

To investigate the healing of the infected incisions, histological analysis was utilized to further evaluate the quality and maturity of the regenerated tissue in the wounds on days 3 and 10 by hematoxylin and eosin (H&E) staining (Fig. 9c). The images showed that there were plenty of inflammatory cells in the control and Tegaderm groups on day 3 without epidermis layer

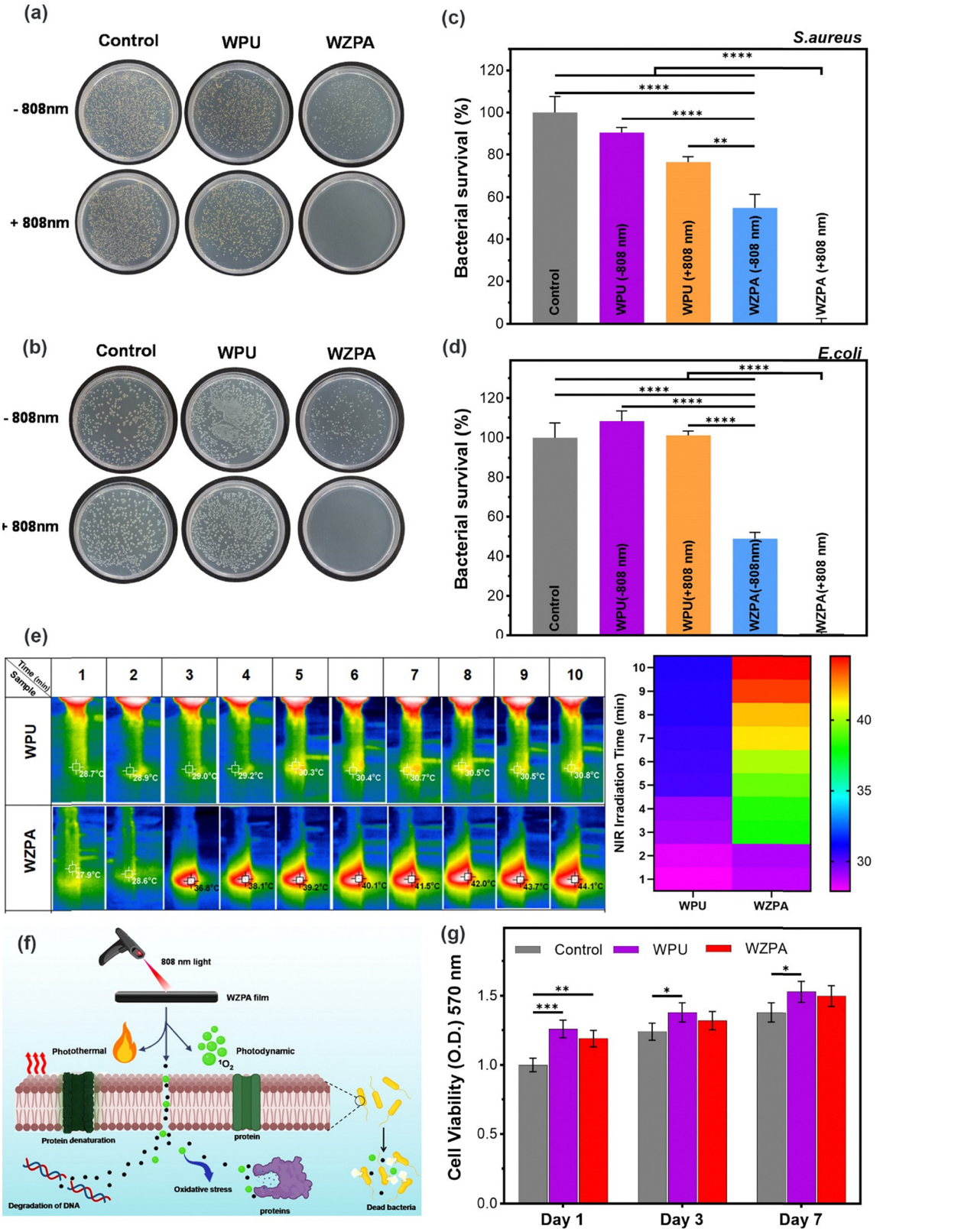

Fig. 8 Plate images depicting the *in vitro* antibacterial effects of the control (PBS), WPU, and WZPA, both with and without NIR irradiation (808 nm, 1 W cm^{-2}) against *S. aureus* (a) and *E. coli* (b). Statistical analysis of bacterial viability assessed through colony counts for *S. aureus* (c) and *E. coli* (d). Data are expressed as mean ± SD, $n = 3$, $^*p < 0.05$, $^{**}p < 0.01$, and $^{**}p < 0.001$. (e) Thermal camera images of WPU and WZPA films under 1 W cm^{-2} continuous NIR light irradiation. (f) Schematic illustration of synergistic effect between PDT and PDA against bacteria cells. (g) Cell viability/proliferation (MTT assay) of L929 fibroblasts seeded on samples in 1, 3 and 7 days ($n = 3$).

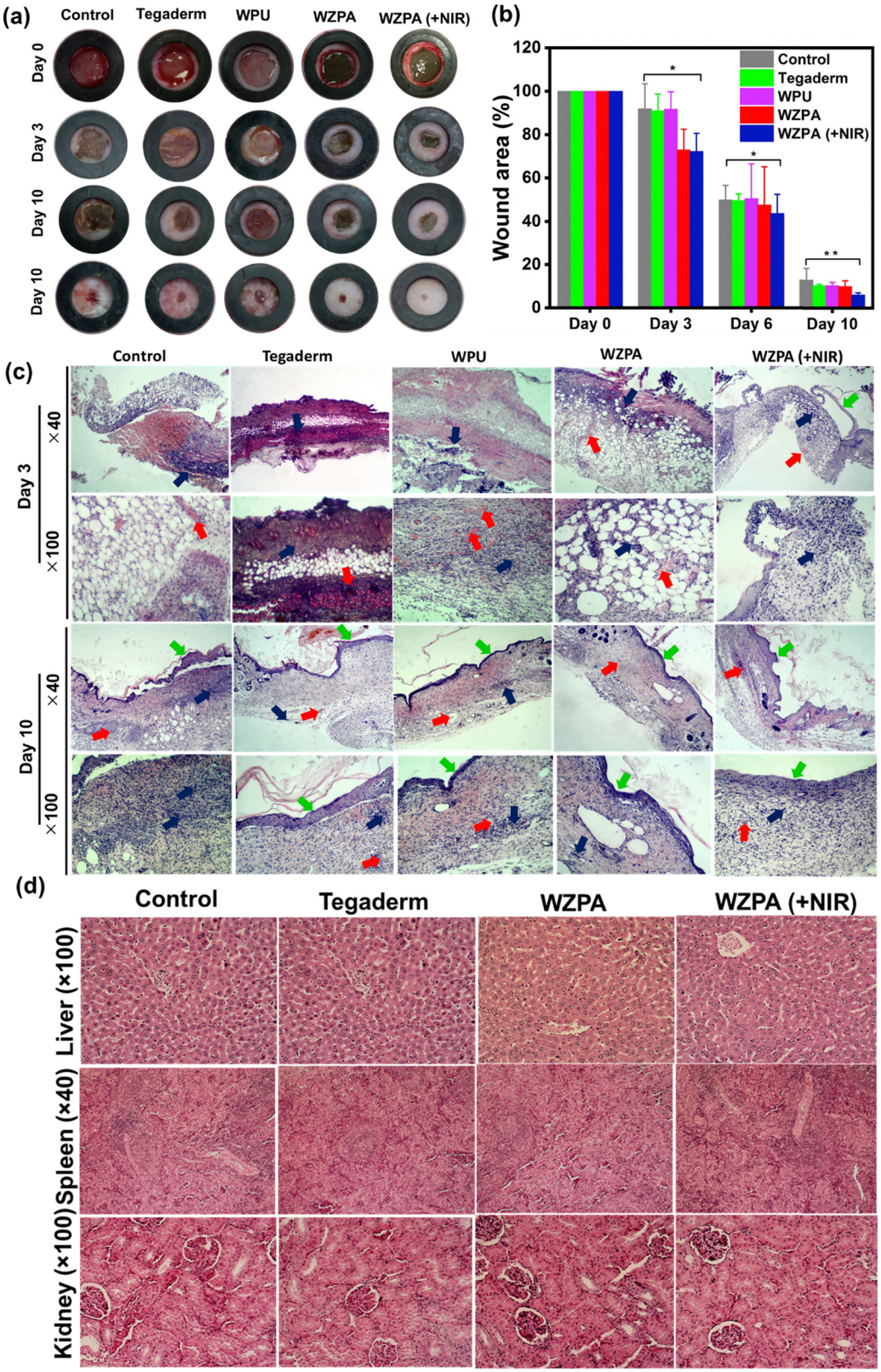

Fig. 9 Photographs of wound contractions using different film dressings at time points of 0, 3, 6, and 10 days (a), changes in wound size after different time points for control, Tegaderm, WPU, WZPA (with/without NIR), as the dressing ($n = 5$; *$p < 0.05$, **$p < 0.01$, the error bars indicate means ± standard deviations) (b), and H&E analysis of the wound tissue obtained from the *S. aureus*-infected rat on (A) days 3 and (B) day 10. Blue, green, and red arrows show inflammatory cells, epidermis layer, and blood vessels, respectively. (c) H&E imaging of liver, spleen, and kidney slices from different groups after the 10th day of treatment (d).

formation. In contrast, the dermis layer formed in the WPU and WZPA (-NIR) groups but a high degree of lymphocyte infiltration without an epithelial layer was observed in the treated groups. There were many blood vessels in the control, WPU, and WZPA (−NIR) groups, indicating the typical first stage of the wound repair process.[96] On the same day, the WZPA (+ NIR) group exhibited partial re-epithelialization on the edge of the wound and the degree of inflammation was less than the other groups. On day 10, the layer of epithelium in the control and Tegaderm groups was immature and did not show good consistency with the dermis layer. Additionally, a considerable amount of lymphocyte infiltration was observed in the control group as well, indicating that severe bacterial infections still occurred. Although the epidermis layer was observed in the WPU group, abundant lobulated lymphocyte infiltration was still seen in the group. In the case of the WZPA (−NIR) group, a layer of epithelial layer was formed and the wound area remarkably decreased compared with the control, WPU, and WZPA (−NIR) groups. The best epithelialization with a mature dermis layer was observed in the WZPA (+NIR) group and the wound reached a normal skin structure, indicating the antibacterial properties of the WZPA and the positive impact of the hyperthermia in the wound healing process.[2] These results demonstrated that the WZPA (+NIR) group would be a promising dressing for skin tissue regeneration and remodeling.

To better evaluate skin tissue repair, quantitative analyses of inflammatory cells and dermis and epidermis thickness were conducted on days 3 and 10 (Fig. 10). On day 3, the thickness of the epidermis in the WZPA + NIR group was significantly greater than that of other groups. In comparison, this thickness in the same group was significantly lower than in the Tegaderm and control groups (Fig. 10a). Fig. 10b shows a significant difference in the dermis thickness of the WZPA + NIR group and the control group. The increased thickness in the control group can be attributed to the infiltration of inflammatory cells, leading to dermis layer thickening (Fig. 10b). These findings illustrate the natural progression of the wound-healing process.[97]

Moreover, the WZPA + NIR group depicted a minimum number of inflammatory cells compared to the other groups, suggesting the antioxidant properties of the WZPA films (Fig. 10c). Fibroblasts and fibrocytes, the primary cells involved in wound repair, were significantly more abundant in the control group than in the WZPA + NIR group on day 3; however, this difference was no longer evident by day 10 (Fig. 10d). Altogether, these quantitative analyses demonstrated that

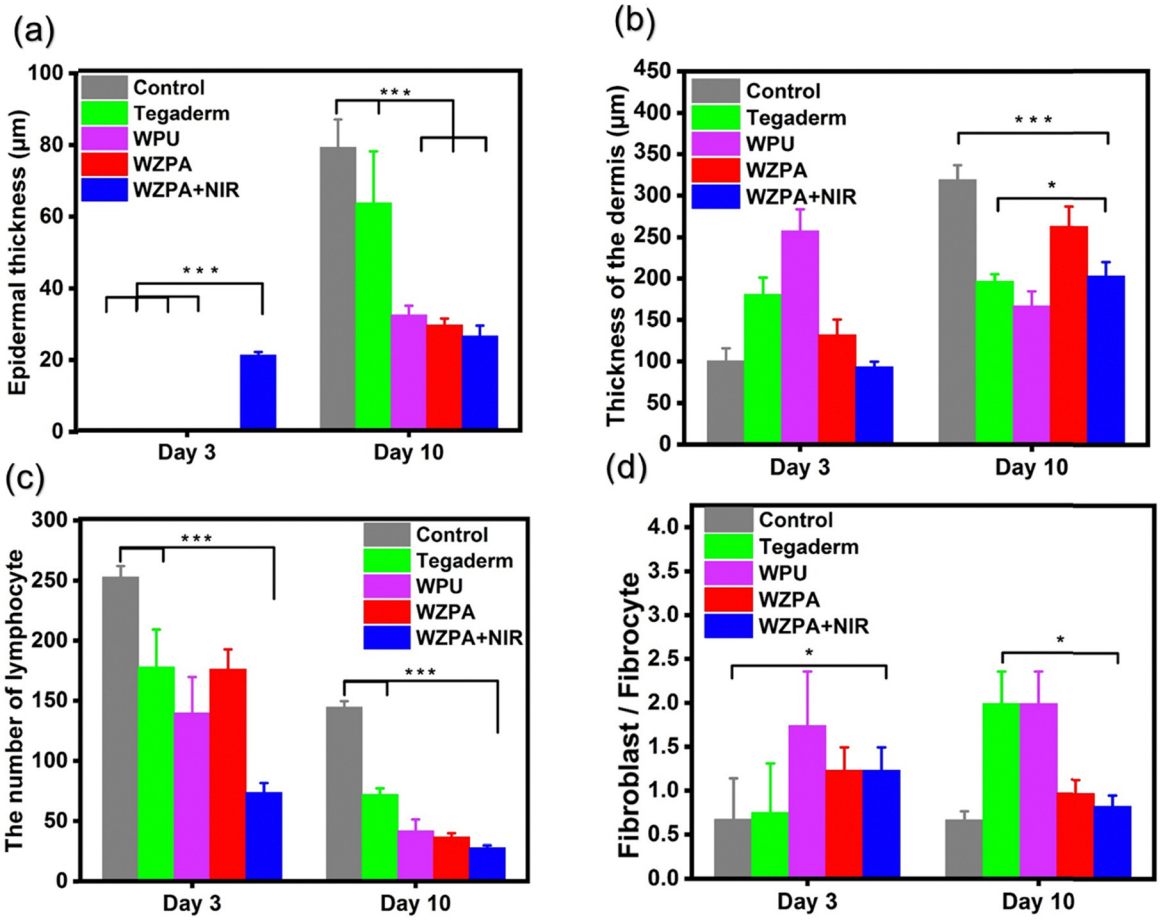

Fig. 10 Quantitative analysis of epithelial coverage (a), thickness of dermis (b), the number of lymphocytes (c), and fibroblasts/fibrocytes (d) (*$p < 0.05$ and ***$p < 0.001$).

the antibacterial activity of the WZPA film, arising from its synergistic photothermal/photodynamic performance along with its antioxidant properties, effectively reduced the inflammatory response and alleviated inflammation, both crucial factors for wound repair and healing.[13,98]

3.1.11. *In vivo* biosafety evaluation of the films. In regenerative medicine, the *in vivo* biocompatibility evaluation of any dressing is of vital importance.[99] To this end, histological analysis of the major organs (livers, kidneys, and spleens) in the WZPA (with and without NIR light)-treated group was used

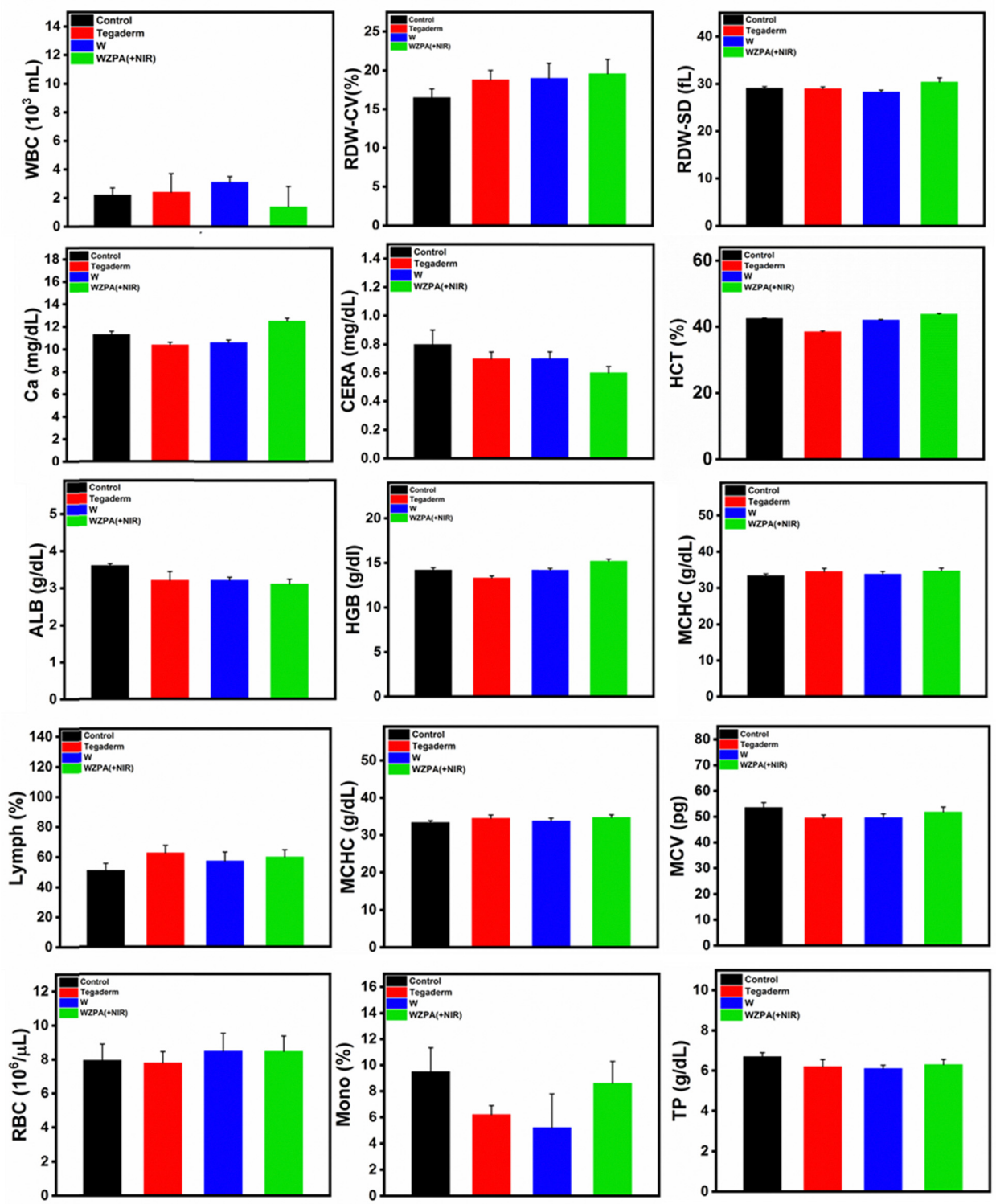

Fig. 11 Hematology and blood biochemical analysis treatment groups (control, Tegaderm, WPU, and WZPA) on day 10.

to assess the biocompatibility of the films. As shown in Fig. 9d, no obvious pathological inflammation or abnormalities were observed in the groups. Hematology and blood biochemical analysis were used to further evaluate the biosafety of the treatment groups (control, Tegaderm, WPU, and WZPA) on day 10. As shown in Fig. 11, there were no significant differences in white blood cells (WBCs), red blood cells (RBCs), monocyte proportion (MONO%) hematocrit test (HCT), mean cell volume (MCV), hemoglobin (HGB), mean corpuscular hemoglobin concentration (MCHC), Ca (mg dL^{-1}), lymphocytes, red blood cell distribution width (RDW%), and renal function parameters [creatinine (CRE)], as well as liver function parameters [albumin (Alb) and total protein (TP)] between the control group and Tegaderm, WPU, and WZPA groups. These results further confirmed the good *in vivo* biocompatibility of the films.

4. Conclusions

This study presents a novel multifunctional waterborne polyurethane (WPU) wound dressing incorporating a hybrid photo nano-sensitizer, ZnO@PDA/Ag, for synergistic photothermal/photodynamic therapy. The nano-sensitizer was engineered through a facile synthesis process involving the coating of zinc oxide (ZnO) nanoparticles with polydopamine (PDA) to enhance biocompatibility and photothermal efficiency, followed by the *in-situ* decoration of silver nanoparticles (Ag NPs) to augment photodynamic activity. The photocatalytic and charge transfer mechanisms were elucidated, highlighting the synergistic effects of surface plasmon resonance of Ag NPs, surface sensitization, and surface passivation effect of PDA in enhancing the photocatalytic activity of the nano-sensitizer system. Additionally, the nanocomposite films showed efficient photothermal capability, which is crucial for photothermal therapy applications. *In vitro* studies demonstrated significant singlet oxygen generation and antibacterial efficacy under NIR irradiation, effectively inhibiting both Gram-negative *E. coli* and Gram-positive *S. aureus* bacteria while maintaining appropriate biocompatibility with L929 fibroblast cells. *In vivo* experiments on an *S. aureus*-infected rat wound model exhibited accelerated wound healing with the ZnO@PDA/Ag-integrated WPU dressing under NIR irradiation, confirming its potential for clinical applications. Histological analysis validated the formation of mature dermis and epidermis layers in treated wounds. Overall, the synergistic photothermal/photodynamic therapy provided by the ZnO@PDA/Ag photo nano-sensitizer shows promise for combating bacterial infections and promoting wound healing, offering a versatile strategy for clinical wound management.

Data availability

Raw data used in preparing the graphs and figures are available upon request.

Conflicts of interest

The authors declare that they have no financial or commercial conflicts of interest.

Acknowledgements

The authors gratefully acknowledge the financial support provided by the University of Isfahan.

References

1 J. Yang, *et al.*, Intelligent wound dressing for simultaneous in situ detection and elimination of pathogenic bacteria, *Acta Biomater.*, 2024, **174**, 177–190.
2 A. Maleki, *et al.*, Multifunctional photoactive hydrogels for wound healing acceleration, *ACS Nano*, 2021, **15**(12), 18895–18930.
3 H. Yang, *et al.*, Multifunctional wound dressing for rapid hemostasis, bacterial infection monitoring and photodynamic antibacterial therapy, *Acta Biomater.*, 2021, **135**, 179–190.
4 S. Sun, *et al.*, Near-infrared light-actuated on-demand botanicals release and hyperthermia by an antibiotic-free polysaccharide-based hydrogel dressing for the synergistic treatment of wound infections, *J. Mater. Chem. B*, 2024, **12**(5), 1307–1316.
5 M. Overchuk, *et al.*, Photodynamic and photothermal therapies: synergy opportunities for nanomedicine, *ACS Nano*, 2023, **17**(9), 7979–8003.
6 Z. Zhou, *et al.*, Reactive oxygen species generating systems meeting challenges of photodynamic cancer therapy, *Chem. Soc. Rev.*, 2016, **45**(23), 6597–6626.
7 D. Jaque, *et al.*, Nanoparticles for photothermal therapies, *Nanoscale*, 2014, **6**(16), 9494–9530.
8 H. Bagheri, *et al.*, Copper-Cysteine Nanostructures for Synergetic Photothermal Therapy and Chemodynamic Therapy of Bacterial Skin Abscesses, *Adv. Ther.*, 2024, 2400099.
9 T. Wang, *et al.*, Cuprous oxide–demethyleneberberine nanospheres for single near-infrared light-triggered photoresponsive-enhanced enzymatic synergistic antibacterial therapy, *J. Mater. Chem. B*, 2023, **11**(8), 1760–1772.
10 M. Zhang, *et al.*, Red Light-Triggered Release of ROS and Carbon Monoxide for Synergistic Antibacterial Application, Available at SSRN 4179196.
11 M. Sheikhi, *et al.*, 4D Printing of Self-Healing, Thermally, and Near-Infrared Light-Responsive Granular Hydrogels with Segmental Directed Movement for Soft Robotic, *ACS Appl. Polym. Mater.*, 2025, **7**(3), 1717–1728.
12 S. Bochani, *et al.*, Injectable, antibacterial, and oxygen-releasing chitosan-based hydrogel for multimodal healing of bacteria-infected wounds, *J. Mater. Chem. B*, 2023, **11**(33), 8056–8068.
13 V. Alinezhad, *et al.*, Antioxidant, hemostatic, and injectable hydrogels with photothermal antibacterial activity to

accelerate full-thickness wound regeneration, *New J. Chem.*, 2024, **48**(17), 7761–7778.
14 Y. Chen, *et al.*, Nanomaterials-based photothermal therapy and its potentials in antibacterial treatment, *J. Controlled Release*, 2020, **328**, 251–262.
15 F. Gao, *et al.*, Titania-coated 2D gold nanoplates as nanoagents for synergistic photothermal/sonodynamic therapy in the second near-infrared window, *Nanoscale*, 2019, **11**(5), 2374–2384.
16 J. Huo, *et al.*, Emerging photothermal-derived multimodal synergistic therapy in combating bacterial infections, *Chem. Soc. Rev.*, 2021, **50**(15), 8762–8789.
17 P. Liu, *et al.*, Concurrent photothermal therapy and photodynamic therapy for cutaneous squamous cell carcinoma by gold nanoclusters under a single NIR laser irradiation, *J. Mater. Chem. B*, 2019, **7**(44), 6924–6933.
18 R. Ma, *et al.*, A triple-mode strategy combining low-temperature photothermal, photodynamic, and chemodynamic therapies for treating infectious skin wounds, *Biomater. Sci.*, 2024, **12**(21), 5521–5533.
19 Y. Tian, R. Guo and W. Yang, Multifunctional nanotherapeutics for photothermal combination therapy of cancer, *Adv. Ther.*, 2018, **1**(8), 1800049.
20 E. Obeng, *et al.*, Multifunctional phototheranostic agent ZnO@ Ag for anti-infection through photothermal/photodynamic therapy, *Front. Chem.*, 2022, **10**, 1054739.
21 H. Fatima, *et al.*, Recent advances in ZnO-based photosensitizers: Synthesis, modification, and applications in photodynamic cancer therapy, *J. Colloid Interface Sci.*, 2022, **621**, 440–463.
22 Y. Huang, *et al.*, Near infrared-driven photocatalytic overall water splitting: Progress and perspective, *Chin. J. Catal.*, 2024, **58**, 105–122.
23 S. Bai, *et al.*, Steering charge kinetics in photocatalysis: intersection of materials syntheses, characterization techniques and theoretical simulations, *Chem. Soc. Rev.*, 2015, **44**(10), 2893–2939.
24 H. J. Nam, *et al.*, A new mussel-inspired polydopamine sensitizer for dye-sensitized solar cells: controlled synthesis and charge transfer, *Chem. – Eur. J.*, 2012, **18**(44), 14000–14007.
25 A. Hezam, *et al.*, Smart plasmonic Ag/Ag2O/ZnO nanocomposite with promising photothermal and photodynamic antibacterial activity under 600 nm visible light illumination, *J. Photochem. Photobiol., A*, 2023, **435**, 114322.
26 D. Franchi and Z. Amara, Applications of sensitized semiconductors as heterogeneous visible-light photocatalysts in organic synthesis, *ACS Sustainable Chem. Eng.*, 2020, **8**(41), 15405–15429.
27 M. Saeed, *et al.*, A simple, green chemistry technology for fabrication of tissue-engineered scaffolds based on mussel-inspired 3D centrifugal spun, *Mater. Sci. Eng., C*, 2021, **121**, 111849.
28 R. Ghodsi, *et al.*, Antioxidant, hemostatic, and injectable hydrogels with photo-thermal antibacterial activity to accelerate full-thickness wound regeneration, *New J. Chem.*, 2024, **48**, 7761–7778.
29 H. Erdoğan, *et al.*, ON/OFF based synergetic plasmonic photothermal drug release approach through core-satellite like mussel-inspired polydopamine nanoparticles, *J. Photochem. Photobiol., B*, 2024, 112889.
30 B. Zhao, *et al.*, Design and application of polyurethane-polydopamine/Ag double-shell microcapsules for enhanced photothermal conversion and incremental energy storage, *Sustainable Mater. Technol.*, 2024, e00895.
31 T. Goel, *et al.*, Synthesis, characterisation of ZnO@ PDA@ Ag nanocomposite: Mechanistic interaction with BSA, photodegradation activity & in vitro cytotoxicity assay on H1299 lung cancer cell line, *Int. J. Biol. Macromol.*, 2024, **283**, 137532.
32 Y. Ouyang, *et al.*, Mussel-inspired ''all-in-one'' sodium alginate/carboxymethyl chitosan hydrogel patch promotes healing of infected wound, *Int. J. Biol. Macromol.*, 2024, **261**, 129828.
33 C. Qi, Y. Zhang and J. Tu, Facile synthesis of ε-poly-L-lysine-conjugated ZnO@ PDA as photothermal antibacterial agents for synergistic bacteria killing and biofilm eradication, *Biochem. Eng. J.*, 2022, **186**, 108569.
34 V. Ball, Polydopamine films: Versatile but interface-dependent coatings, *Nanotechnol. Rev.*, 2024, **13**(1), 20230216.
35 X. He, *et al.*, Polydopamine, harness of the antibacterial potentials-A review, *Mater. Today Bio*, 2022, **15**, 100329.
36 A. Mohammadi, *et al.*, Silver (I) complex with a Schiff base ligand extended waterborne polyurethane: A developed strategy to obtain a highly stable antibacterial dispersion impregnated with in situ formed silver nanoparticles, *Chem. Eng. J.*, 2020, **381**, 122776.
37 C. E. Tas, *et al.*, Photothermal waterborne polydopamine/polyurethanes with light-to-heat conversion properties, *ACS Appl. Polym. Mater.*, 2021, **3**(8), 3929–3940.
38 B. Alkan-Taş, *et al.*, NIR-responsive waterborne polyurethane-polydopamine coatings for light-driven disinfection of surfaces, *Prog. Org. Coat.*, 2022, **164**, 106669.
39 F. Lu, *et al.*, Black phosphorus quantum dots encapsulated in anionic waterborne polyurethane nanoparticles for enhancing stability and reactive oxygen species generation for cancer PDT/PTT therapy, *J. Mater. Chem. B*, 2020, **8**(46), 10650–10661.
40 A. Mohammadi, *et al.*, Antibacterial waterborne polyurethane coatings impregnated with in-situ formed and capped silver nanoparticles via p-sulfonatocalix [4] arene, *Prog. Org. Coat.*, 2023, **180**, 107551.
41 D. Fuentes-López, *et al.*, The growth of Escherichia coli cultures under the influence of pheomelanin nanoparticles and a chelant agent in the presence of light, *PLoS One*, 2022, **17**(3), e0265277.
42 G. Boso, *et al.*, Time-resolved singlet-oxygen luminescence detection with an efficient and practical semiconductor single-photon detector, *Biomed. Opt. Express*, 2016, **7**(1), 211–224.
43 Q. Tian, *et al.*, Hydrophilic Cu9S5 nanocrystals: a photothermal agent with a 25.7% heat conversion efficiency for photothermal ablation of cancer cells in vivo, *ACS Nano*, 2011, **5**(12), 9761–9771.

44 Y. Liang, *et al.*, Adhesive hemostatic conducting injectable composite hydrogels with sustained drug release and photothermal antibacterial activity to promote full-thickness skin regeneration during wound healing, *Small*, 2019, **15**(12), 1900046.
45 L. Qiao, *et al.*, Antibacterial conductive self-healing hydrogel wound dressing with dual dynamic bonds promotes infected wound healing, *Bioact. Mater.*, 2023, **30**, 129–141.
46 G. Nagaraju, *et al.*, Electrochemical heavy metal detection, photocatalytic, photoluminescence, biodiesel production and antibacterial activities of Ag–ZnO nanomaterial, *Mater. Res. Bull.*, 2017, **94**, 54–63.
47 V. Fedorenko, *et al.*, Application of polydopamine functionalized zinc oxide for glucose biosensor design, *Polymers*, 2021, **13**(17), 2918.
48 H. Luo, *et al.*, Facile synthesis of novel size-controlled antibacterial hybrid spheres using silver nanoparticles loaded with poly-dopamine spheres, *RSC Adv.*, 2015, **5**(18), 13470–13477.
49 J. Liao, *et al.*, Antibacterial Performance of a Mussel-Inspired Polydopamine-Treated Ag/Graphene Nanocomposite Material, *Materials*, 2019, **12**(20), 3360.
50 S. Talam, S. R. Karumuri and N. Gunnam, Synthesis, characterization, and spectroscopic properties of ZnO nanoparticles. International Scholarly Research Notices, 2012.
51 S. Yedurkar, C. Maurya and P. Mahanwar, Biosynthesis of zinc oxide nanoparticles using ixora coccinea leaf extract—a green approach, *Open J. Synth. Theory Appl.*, 2016, **5**(1), 1–14.
52 L. Huang, *et al.*, Study on synthesis and antibacterial properties of Ag NPs/GO nanocomposites, *J. Nanomater.*, 2016, DOI: 10.1155/2016/5685967.
53 A. Mohammadi, *et al.*, A high-efficient antibacterial and biocompatible polyurethane film with Ag@ rGO nanostructures prepared by microwave-assisted method: Physicochemical and dermal wound healing evaluation, *Heliyon*, 2023, **9**(11), e21783.
54 S. Kantipudi, *et al.*, Enhanced wound healing activity of Ag–ZnO composite NPs in Wistar Albino rats, *IET Nanobiotechnol.*, 2018, **12**(4), 473–478.
55 R. Al-Gaashani, *et al.*, XPS and optical studies of different morphologies of ZnO nanostructures prepared by microwave methods, *Ceram. Int.*, 2013, **39**(3), 2283–2292.
56 K. P. Wai, *et al.*, In situ immobilization of silver on polydopamine-coated composite membrane for enhanced antibacterial properties, *J. Water Process Eng.*, 2020, **33**, 100989.
57 R. A. Zangmeister, T. A. Morris and M. J. Tarlov, Characterization of polydopamine thin films deposited at short times by autoxidation of dopamine, *Langmuir*, 2013, **29**(27), 8619–8628.
58 H. A. Lee, E. Park and H. Lee, Polydopamine and its derivative surface chemistry in material science: a focused review for studies at KAIST, *Adv. Mater.*, 2020, **32**(35), 1907505.
59 L. C. Almeida, *et al.*, Electrosynthesis of polydopamine-ethanolamine films for the development of immunosensing interfaces, *Sci. Rep.*, 2021, **11**(1), 2237.
60 R. Batul, *et al.*, Polydopamine nanosphere with in-situ loaded gentamicin and its antimicrobial activity, *Molecules*, 2020, **25**(9), 2090.
61 K. Choi, T. Kang and S.-G. Oh, Preparation of disk shaped ZnO particles using surfactant and their PL properties, *Mater. Lett.*, 2012, **75**, 240–243.
62 Y. Mongy and T. Shalaby, Green synthesis of zinc oxide nanoparticles using Rhus coriaria extract and their anticancer activity against triple-negative breast cancer cells, *Sci. Rep.*, 2024, **14**(1), 13470.
63 H.-K. Chin, *et al.*, Polydopamine-mediated Ag and ZnO as an active and recyclable SERS substrate for rhodamine b with significantly improved enhancement factor and efficient photocatalytic degradation, *Appl. Sci.*, 2021, **11**(11), 4914.
64 Y. Liu, S. Wei and W. Gao, Ag/ZnO heterostructures and their photocatalytic activity under visible light: effect of reducing medium, *J. Hazard. Mater.*, 2015, **287**, 59–68.
65 S. A. Ansari, *et al.*, Biogenic synthesis, photocatalytic, and photoelectrochemical performance of Ag–ZnO nanocomposite, *J. Phys. Chem. C*, 2013, **117**(51), 27023–27030.
66 A. Guo, *et al.*, Singlet oxygen mediated efficient photocatalytic degradation of rhodamine B and disinfection by ZnO@ PDA/Ag-Ag2O nanocomposite under LED light, *J. Alloys Compd.*, 2022, **928**, 167138.
67 C. Jia, *et al.*, Interface-engineered plasmonics in metal/semiconductor Heterostructures, *Adv. Energy Mater.*, 2016, **6**(17), 1600431.
68 F. Guo, *et al.*, Z-scheme heterojunction g-C3N4@ PDA/BiOBr with biomimetic polydopamine as electron transfer mediators for enhanced visible-light driven degradation of sulfamethoxazole, *Chem. Eng. J.*, 2020, **386**, 124014.
69 L. Ye, *et al.*, Two different roles of metallic Ag on Ag/AgX/BiOX (X= Cl, Br) visible light photocatalysts: surface plasmon resonance and Z-scheme bridge, *ACS Catal.*, 2012, **2**(8), 1677–1683.
70 R. Xue, *et al.*, Visible and infrared solar radiation upconversion for water splitting via a surface plasmon-passivated strategy, *J. Mater. Chem. A*, 2022, **10**(7), 3771–3781.
71 Y. Liu, K. Ai and L. Lu, Polydopamine and its derivative materials: synthesis and promising applications in energy, environmental, and biomedical fields, *Chem. Rev.*, 2014, **114**(9), 5057–5115.
72 Y. Kim, *et al.*, Efficient photocatalytic production of hydrogen by exploiting the polydopamine-semiconductor interface, *Appl. Catal., B*, 2021, **280**, 119423.
73 G. V. Lowry, *et al.*, Guidance to improve the scientific value of zeta-potential measurements in nanoEHS, *Environ. Sci.:-Nano*, 2016, **3**(5), 953–965.
74 A. Mohammadi, M. Barikani and M. Barmar, Synthesis and investigation of thermal and mechanical properties of in situ prepared biocompatible Fe_3O_4/polyurethane elastomer nanocomposites, *Polym. Bull.*, 2015, **72**, 219–234.
75 X.-Y. Ma and W.-D. Zhang, Effects of flower-like ZnO nanowhiskers on the mechanical, thermal and antibacterial properties of waterborne polyurethane, *Polym. Degrad. Stab.*, 2009, **94**(7), 1103–1109.

76 Z. Yin, *et al.*, Thermal stability, surface wettability and mechanical behavior of highly ordered ZnO-doped thermoplastic polyurethane films with hierarchically porous structures, *J. Appl. Polym. Sci.*, 2021, **138**(38), 50989.
77 J. Pavličević, *et al.*, The influence of ZnO nanoparticles on thermal and mechanical behavior of polycarbonate-based polyurethane composites, *Composites, Part B*, 2014, **60**, 673–679.
78 A. Mohammadi, *et al.*, Aqueous dispersion of polyurethane nanocomposites based on calix [4] arenes modified graphene oxide nanosheets: preparation, characterization, and anti-corrosion properties, *Chem. Eng. J.*, 2018, **349**, 466–480.
79 V. Alinezhad, *et al.*, Engineering a platelet-rich plasma-based multifunctional injectable hydrogel with photothermal, antibacterial, and antioxidant properties for skin regeneration, *Biomater. Sci.*, 2023, **11**(17), 5872–5892.
80 C. Xie, *et al.*, Electroactive hydrogels with photothermal/photodynamic effects for effective wound healing assisted by polydopamine-modified graphene oxide, *ACS Appl. Mater. Interfaces*, 2023, **15**(36), 42329–42340.
81 Y. Liu, *et al.*, Silver nanoparticle-embedded hydrogel as a photothermal platform for combating bacterial infections, *Chem. Eng. J.*, 2020, **382**, 122990.
82 X. Qi, *et al.*, Engineering robust Ag-decorated polydopamine nano-photothermal platforms to combat bacterial infection and prompt wound healing, *Adv. Sci.*, 2022, **9**(11), 2106015.
83 Z. Li, *et al.*, Architecting polyelectrolyte hydrogels with Cu-assisted polydopamine nanoparticles for photothermal antibacterial therapy, *Mater. Today Bio*, 2022, **15**, 100264.
84 S. Chen, *et al.*, Janus polyurethane sponge as an antibiofouling, antibacterial, and exudate-managing dressing for accelerated wound healing, *Acta Biomater.*, 2023, **171**, 428–439.
85 Z. Yuan, *et al.*, Near-infrared light-triggered nitric-oxide-enhanced photodynamic therapy and low-temperature photothermal therapy for biofilm elimination, *ACS Nano*, 2020, **14**(3), 3546–3562.
86 K. Zha, *et al.*, Three-Step Regenerative Strategy: Multifunctional Bilayer Hydrogel for Combined Photothermal/Photodynamic Therapy to Promote Drug-Resistant Bacteria-Infected Wound Healing, *Adv. Funct. Mater.*, 2024, **34**(2), 2308145.
87 S. Bochani, *et al.*, Injectable antibacterial gelatin-based hydrogel incorporated with two-dimensional nanosheets for multimodal healing of bacteria-infected wounds, *ACS Appl. Bio Mater.*, 2022, **5**(9), 4435–4453.
88 N. Masood, *et al.*, Silver nanoparticle impregnated chitosan-PEG hydrogel enhances wound healing in diabetes induced rabbits, *Int. J. Pharm.*, 2019, **559**, 23–36.
89 K. Zhou, *et al.*, Hybrid Ag nanoparticles/polyoxometalate-polydopamine nano-flowers loaded chitosan/gelatin hydrogel scaffolds with synergistic photothermal/chemodynamic/Ag+ anti-bacterial action for accelerated wound healing, *Int. J. Biol. Macromol.*, 2022, **221**, 135–148.
90 Y. Jiang, *et al.*, Controlled release of silver ions from Ag NPss using a hydrogel based on konjac glucomannan and chitosan for infected wounds, *Int. J. Biol. Macromol.*, 2020, **149**, 148–157.
91 C. Mao, *et al.*, Local photothermal/photodynamic synergistic therapy by disrupting bacterial membrane to accelerate reactive oxygen species permeation and protein leakage, *ACS Appl. Mater. Interfaces*, 2019, **11**(19), 17902–17914.
92 L. S. Lin, *et al.*, Simultaneous Fenton-like ion delivery and glutathione depletion by MnO2-based nanoagent to enhance chemodynamic therapy, *Angew. Chem.*, 2018, **130**(18), 4996–5000.
93 H. Bagheri, *et al.*, Copper-Cysteine Nanostructures for Synergetic Photothermal Therapy and Chemodynamic Therapy of Bacterial Skin Abscesses, *Adv. Ther.*, 2024, **7**(8), 2400099.
94 S. A. A. Najafabadi, A. Mohammadi and A. Z. Kharazi, Polyurethane nanocomposite impregnated with chitosan-modified graphene oxide as a potential antibacterial wound dressing, *Mater. Sci. Eng., C*, 2020, **115**, 110899.
95 M. Składanowski, *et al.*, Evaluation of cytotoxicity, immune compatibility and antibacterial activity of biogenic silver nanoparticles, *Med. Microbiol. Immunol.*, 2016, **205**(6), 603–613.
96 G. C. Gurtner, *et al.*, Wound repair and regeneration, *Nature*, 2008, **453**(7193), 314–321.
97 A. Shrivastav, *et al.*, In vivo models for assesment of wound healing potential: A systematic review, *Wound Med.*, 2018, **20**, 43–53.
98 B. Qiao, *et al.*, ROS-responsive hydrogels with spatiotemporally sequential delivery of antibacterial and anti-inflammatory drugs for the repair of MRSA-infected wounds, *Regener. Biomater.*, 2024, **11**, rbad110.
99 Y. Lin, *et al.*, Recent advances in nano-formulations for skin wound repair applications, *Drug Des., Dev. Ther.*, 2022, 2707–2728.

